

JWST Captures Growth of Aromatic Hydrocarbon Dust Particles in the Extremely Metal-poor Galaxy Sextans A

Elizabeth J. Tarantino^{1*}, Julia Roman-Duval¹, Karin M. Sandstrom²,
J.-D. T. Smith³, Cory M. Whitcomb³, Bruce T. Draine⁴, Martha L. Boyer¹,
J  r  my Chasten  t⁵, Ryan Chown^{6, 7}, Christopher J. R. Clark⁸, Karl D. Gordon¹,
Brandon S. Hensley⁹, Thomas S.-Y. Lai¹⁰, Christina W. Lindberg^{11, 1, 12},
Kristen B. W. McQuinn^{1, 13}, Max J. B. Newman¹, O. Grace Telford^{14, 4, 15},
Dries Van De Putte¹⁶, Benjamin F. Williams¹⁷

¹Space Telescope Science Institute, 3700 San Martin Drive, Baltimore, MD 21218, USA.

²Department of Astronomy & Astrophysics, University of California, San Diego, La Jolla, CA 92093, USA.

³Ritter Astrophysical Research Center, Department of Physics & Astronomy, University of Toledo, Toledo, OH 43606, USA.

⁴Department of Astrophysical Sciences, Princeton University, USA 08544.

⁵Sterrenkundig Observatorium, Universiteit Gent, Krijgslaan 281 S9, B-9000 Gent, Belgium.

⁶Faculty of Computer Science & Technology, Algoma University, Sault Ste. Marie, ON P6A 2G4, Canada.

⁷Department of Astronomy, The Ohio State University, 140 West 18th Avenue, Columbus, OH 43210, USA.

⁸AURA for the European Space Agency, Space Telescope Science Institute, 3700 San Martin Drive, Baltimore, MD 21218, USA.

⁹Jet Propulsion Laboratory, California Institute of Technology, 4800 Oak Grove Drive, Pasadena, CA 91109, USA.

¹⁰IPAC, California Institute of Technology, 1200 East California Boulevard, Pasadena, CA 91125, USA.

¹¹Center for Astrophysics | Harvard & Smithsonian, 60 Garden St., Cambridge, MA 02138, USA.

¹²The William H. Miller III Department of Physics & Astronomy, Bloomberg Center for Physics and Astronomy, Johns Hopkins University, 3400 N. Charles Street, Baltimore, MD 21218, USA.

¹³Department of Physics and Astronomy, Rutgers the State University of New Jersey, 136 Frelinghuysen Rd., Piscataway, NJ, 08854, USA.

¹⁴Department of Physics and Astronomy, University of Utah, 270 S 1400 E, Salt Lake City, UT 84112, USA.

¹⁵The Observatories of the Carnegie Institution for Science, 813 Santa Barbara Street, Pasadena, CA 91101, USA.

¹⁶Department of Physics & Astronomy, The University of Western Ontario, London ON N6A 3K7, Canada.

¹⁷Department of Astronomy, University of Washington, Box 351580, U.W., Seattle, WA 98195-1580, USA.

Abstract

The mid-infrared spectrum of star-forming, high metallicity galaxies is dominated by emission features from aromatic and aliphatic bonds in small carbonaceous dust grains, often referred to as polycyclic aromatic hydrocarbons (PAHs). In metal-poor galaxies, the abundance of PAHs relative to the total dust sharply declines, but the origin of this deficit is unknown. We present JWST observations that detect and resolve emission from PAHs in the 7% Solar metallicity galaxy Sextans A, representing the lowest metallicity detection of PAH emission to date. In contrast to higher metallicity galaxies, the clumps of PAH emission are compact (0.5-1.5'' or 3-10 pc), which explains why PAH emission evaded detection by lower resolution instruments like Spitzer. Ratios between the 3.3, 7.7, and 11.3 μm PAH features indicate that the PAH grains in Sextans A are small and neutral, with no evidence of significant processing from the hard radiation fields within the galaxy. These results favor inhibited grain growth over enhanced destruction as the origin of the low PAH abundance in Sextans A. The compact clumps of PAH emission are likely active sites of in-situ PAH growth within a dense, well-shielded phase of the interstellar medium. Our results show that PAHs can form and survive in extremely metal-poor environments common early in the evolution of the Universe.

1 Introduction

The mid-infrared (MIR) spectrum of interstellar material is dominated by broad emission features, at 3.3, 3.4, 5.3, 5.6, 6.3, 7.7, 8.6, 11.3, 12.6, and 17.3 μm , that are attributed to vibrational modes of carbonaceous nanoparticles often referred to as polycyclic aromatic hydrocarbons (PAHs¹; [4–8]). Because PAH features are excited by UV photons and suffer minimally from extinction, they are bright in regions powered by young massive stars, accounting for 5-20% of the total IR luminosity of high metallicity galaxies [9, 10]. As a result, PAH emission is used as a tracer of star formation rate [SFR; 11–14] and molecular gas [15–18] in nearby and distant galaxies. In neutral gas, PAHs drive the heating through the photoelectric effect [19–21] and regulate the ionization balance via nanoparticle-mediated recombination of ions and electrons.

One of the main results from previous IR telescopes, such as the Spitzer Space Telescope, is the strong dependence of PAH flux on metallicity [e.g., 22–38]. The fraction of PAHs in the overall dust mass drastically decreases around a metallicity of $12 + \log(\text{O}/\text{H}) \sim 8.2$ ($\sim 30\% Z_{\odot}$) [29, 37, 38]. While the origin of this PAH deficit is unknown, it is generally attributed to either enhanced destruction and/or suppressed formation of these small grains. In the enhanced destruction scenario, low dust abundances in metal-poor systems may lead to reduced shielding of PAHs from far-ultraviolet (FUV) radiation [39]. PAH compounds are more fragile than larger dust grains [40], which can result in preferential destruction of PAHs in these metal-poor systems [24–27, 32, 34]. Similarly, PAHs may also be destroyed through interactions with electrons in ionized gas [29, 40] or interstellar shocks [41]. The other scenario to explain the PAH deficit at low metallicity is through the suppression of formation mechanisms. PAH growth in the ISM may be inhibited at low metallicities due to an under-abundance of carbon, and/or less dense gas available to support efficient grain growth [38, 42–44]. Another theory suggests that PAHs form through the shattering of larger dust grains, and that reduced dust abundances therefore suppress the creation of PAHs from fragmentation [45, 46].

Understanding the PAH deficit at low metallicity is therefore directly tied to the formation, destruction, and overall lifecycle of these small grains. Establishing a framework for PAHs at low metallicities is thus vital for interpreting PAH observations, particularly at high redshift where detections are becoming more common and average metallicities are lower [e.g. 12, 14, 47–50]. While observations with *Spitzer* made tremendous progress in revealing the PAH deficit at low metallicity, the enhanced sensitivity, spectral coverage, and spatial resolution of JWST are now transforming our view of nearby galaxies. Several JWST spectroscopic and photometric programs have targeted metal-poor systems, but PAHs have remained undetected below $Z < 13\% Z_{\odot}$ [51–59].

¹The particles have a mixed aromatic-aliphatic composition [1–3], but we refer to them as PAHs for simplicity.

In this work, we leverage the exquisite sensitivity and resolution of JWST to target the nearby, star-forming, metal-poor, dwarf irregular galaxy Sextans A to detect and characterize PAH emission at very low metallicity. Sextans A has an oxygen abundance of $12 + \log(\text{O}/\text{H}) = 7.54$ [60], which translates to a 7% Solar metallicity when assuming $12 + \log(\text{O}/\text{H}) = 8.69$ for the Sun [61]. Sextans A resides at the outer edge of the Local Group, at a distance of 1.4 Mpc [62, 63]. Like many dwarf irregular galaxies, the mass of Sextans A is dominated by atomic gas, with a $M_{\text{HI}} = 6.2 \times 10^7 M_{\odot}$ [64] and a stellar mass of $M_{\star} = 4.4 \times 10^7 M_{\odot}$ [65]. The UV-derived SFR of is $\text{SFR} = 1.2 \times 10^{-2} M_{\odot} \text{ yr}^{-1}$ [66], indicating there is ongoing star formation within the galaxy. Sextans A has a previous detection of cold dust from *Herschel* [67], making it an ideal target to detect PAH emission with JWST.

2 Discovery of compact PAH clumps at 7% Solar metallicity

We obtained photometry of Sextans A with JWST NIRCам and MIRI imaging, focusing on filters centered on PAH emission— F335M, F770W, and F1130W— as well as flanking filters to estimate the continuum level (see Section 3.1 for details). The observations consist of a single NIRCам and MIRI deep field towards the brightest star-forming region in Sextans A with a previous dust detection [27, 67], marked by the magenta rectangle in the optical image of Sextans A shown in Figure 1a. The combined NIRCам and MIRI photometric imaging is presented as a multi-color image in 1b, where the region of brightest PAH emission is encompassed by the green rectangle. The bottom panels (c. – e.) zoom in on this region, with each PAH filter shown in green and the flanking continuum filters in red and blue. The green color indicates enhanced emission at the 3.3, 7.7, and 11.3 μm PAH features, demonstrating the presence of PAHs in this extremely low-metallicity galaxy. The emission from PAHs is compact, arising from $1 - 1.5''$, or $4 - 10$ pc clumps.

To confirm the detection of PAHs in Sextans A, we analyze the spectral energy distribution (SED) of the brightest clump of PAH emission in Figure 2 (encircled in Panels 1c.–e.). We extract the flux of all filters from the JWST observations and compare the observed SED to MIR model of dust emission spectra from Draine et al. [69] (hereafter D21) and near-infrared stellar spectra from PHOENIX models [70] (see 3.4 for more details). This SED shows an uptick in the flux for each PAH filter (green) relative to the bracketing continuum filters (magenta), indicating PAH emission. The detection is seen in the three independent PAH features: 3.3, 7.7, and 11.3 μm , ensuring that it is robust and not from a spurious high redshift galaxy. At 7% Solar metallicity, these observations are the lowest metallicity resolved detection of PAH emission to date.

We develop a continuum subtraction method that removes the stellar and hot dust continuum contribution to each PAH filter in order to isolate the PAH flux. This method expands on previous work with the F335M NIRCам filter from Sandstrom et al. [71] to also include an approach for the MIRI filters and is described in detail in Section 3.1.4. Figure 3a shows an RGB 3-color image of the the stellar and hot dust continuum while Figure 3b shows the continuum-subtracted PAH flux at 11.3 (red), 7.7 (green) and 3.3 (blue) μm . We also zoom in on the green rectangle highlighted in Figure 1 and show the continuum-subtracted PAH flux for each feature in Figure 4.

As Figures 3 and 4 show, the clumps of PAH emission exhibit hierarchical structure, where smaller clumps are nested within larger ones. We therefore use dendrograms to identify and measure the properties of the PAH clumps (see Section 3.3 for more details). A PAH clump is defined by a 3σ detection in all three continuum-subtracted PAH images, ensuring the detection is robust and not due to an interloping galaxy. The resulting clump envelopes and labels are outlined in white in Figure 3. Background galaxies appear bright in only a single band (e.g., red at 11.3 μm), demonstrating the need for 3σ detections across all PAH bands. The properties of each clump, including the position, integrated continuum subtracted PAH flux, and size are given in Table 1. The average deconvolved radius of these clumps are $0.3''$ (2 pc) and range from $0.18 - 0.72''$ (1.22 – 4.89 pc). Since the spatial resolution of the data (after convolving to 15 μm resolution) is $0.488''$ (3.3 pc), many of the clumps are unresolved even at the exquisite resolution of JWST.

The dendrogram analysis as well as Figures 3 & 4 all show that the PAH clumps in Sextans A are small and compact, about $0.5 - 1.5''$, or $4 - 10$ pc in diameter. Higher metallicity galaxies, in contrast, have PAH emitting regions as large as 500 pc or more [e.g., 10, 74–76]. Even in the 20% Solar metallicity Small Magellanic Cloud (SMC) [77], typical sizes of PAH emitting regions are comparable to molecular cloud sizes, around 25 pc or greater [35, 36, 43, 78]. The small size of the PAH clumps in Sextans A is

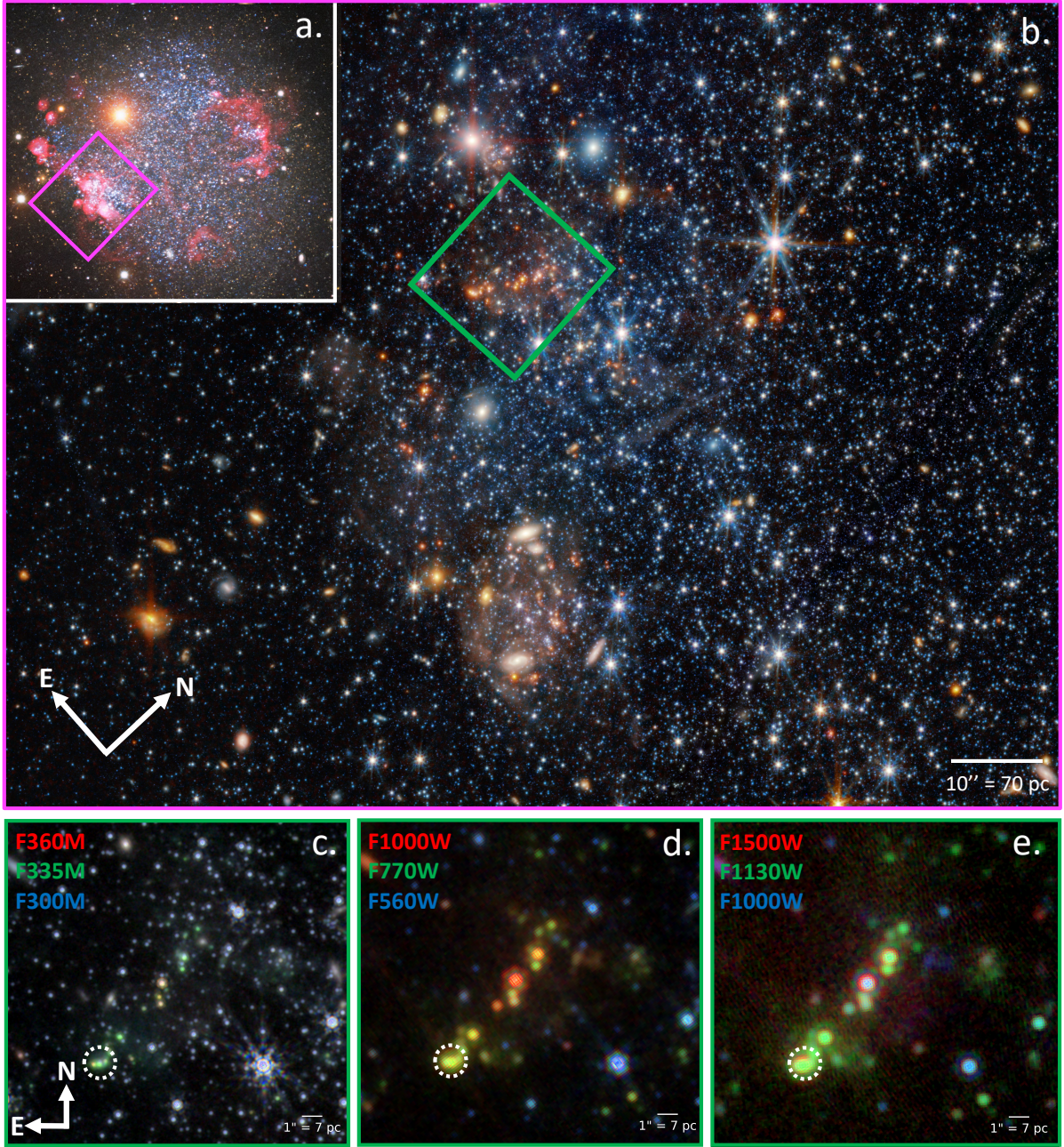


Fig. 1 JWST NIRCam and MIRI photometry of Sextans A reveals emission from PAHs a.) Optical image of Sextans A (Credit: KPNO/NOIRLab/NSF/AURA) with the JWST field outlined in magenta. b.) JWST color composite image of Sextans A (Blue: F115W, Cyan: F150W + F200W, Green: F335M, Yellow: F560W, Orange: F770W, Red: F1000W; Credit: A. Pagan, STScI). The region of brightest PAH emission is outlined in green. c.–e.) 3-color zoom-ins on this region, with the PAH filter in green and adjacent continuum filters in red and blue (c. Red: F360M, Green: F335M, Blue: F300M; d. Red: F1000W, Green: F770W, Blue: F560W; e. Red: F1500W, Green: F1130W, Blue: F1000W). We apply the Lupton RGB algorithm [68] to visualize the high dynamic range of the JWST data, using the same asinh stretch and scaling for all panels. The compact green clumps trace enhanced emission from the PAH 3.3, 7.7, and 11.3 μm features, with the brightest clump highlighted by a circle.

instead reminiscent of the tiny cores of molecular gas found in $\lesssim 13\%$ Solar metallicity galaxies WLM and Sextans B [79–82]. Given that PAHs and CO are well correlated in high metallicity galaxies [16, 18], we predict the small clumps of PAH emission trace the molecular cores in Sextans A and share similar conditions for formation and survival. Because the dust-to-gas ratio decreases with metallicity [39, 83, 84], a larger gas column is required to reach the same A_V (a measure of the dust shielding) as in a more

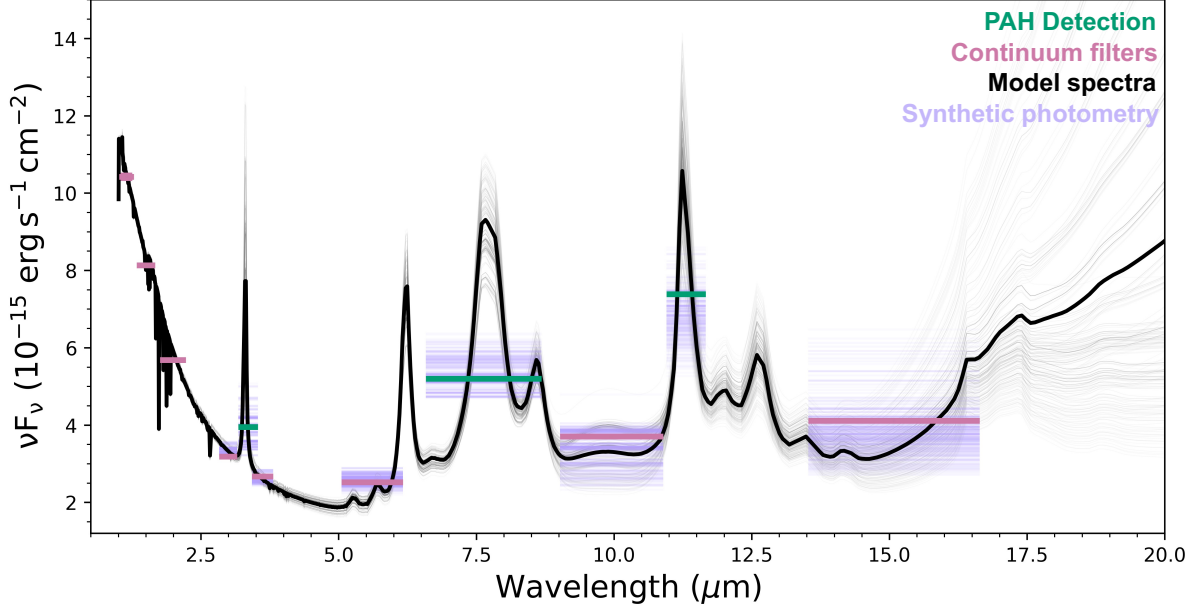


Fig. 2 SED of the brightest clump of PAH emission in Sextans A. The flux from clump 1 (encircled in Figure 1c–e) is shown by magenta and green horizontal lines, with green denoting the PAH-centered filters (F335M, F770W, F1130W). Line widths indicate the wavelength range where the filter transmission falls to 50% of its maximum. Errorbars are smaller than the linewidth. The excess flux in the PAH filters (green) relative to the continuum filters (magenta) demonstrates the detection of PAHs. PHOENIX stellar models [70] and D21 PAH/dust emission spectral models that fit the data within uncertainties are presented as the gray spectra, with the transparency scaled by the χ^2 and the average spectrum presented in black. The spread in models illustrates how different ISM conditions (e.g., radiation field, neutral gas column density, PAH size and charge distribution) can produce equally valid fits to the photometric data (see Section 3.4). The purple horizontal lines show the synthetic photometry of these models for direct comparison with the observations.

metal-rich ISM [85–87], leading to an overall smaller physical scale where dust shielding is effective. The small size of the PAH clumps therefore suggests that dust shielding is playing an important role in survival and growth of PAHs.

To quantify the PAH abundance in Sextans A, we calculate the ratio of the summed PAH feature luminosities to the total infrared luminosity ($\Sigma\text{PAH}/\text{TIR}$), which captures the fraction of infrared power emitted by PAH features [e.g., 10, 34, 38]. This ratio serves as a proxy for q_{PAH} , the fraction of the overall dust budget in PAHs by mass, with small dependence on the radiation field strength at very high radiation fields. In Figure 5, we plot $\Sigma\text{PAH}/\text{TIR}$ for Sextans A (this work) and compare to a sample of low metallicity galaxies presented in Hunt et al. [34] and the higher metallicity SINGS (The SIRTf Nearby Galaxies Survey) sample [10, 88]. We follow the procedure in Draine et al. [29] to calculate the total infrared luminosity in Sextans A, assuming a distance of 1.4 Mpc [63]. We use the FIR fluxes from *Spitzer* and *Herschel* reported in the $32'' \times 32''$ “sf-3” region in Shi et al. [67], which is displayed as the circle in Figure 3. After applying a 3σ signal-to-noise ratio (SNR) cut to the 3.3, 7.7, and 11.3 μm continuum subtracted PAH data, we sum these three PAH features in the “sf-3” region defined in Shi et al. [67] to calculate ΣPAH and plot $\Sigma\text{PAH}/\text{TIR} = 0.0015$ in Figure 5. We also overplot and extrapolate the fitted trend from Whitcomb et al. [38], which fits $\Sigma\text{PAH}/\text{TIR}$ across the metallicity gradients of three nearby galaxies M101, NGC 628, and NGC 2403. The Sextans A $\Sigma\text{PAH}/\text{TIR}$ measurement is in agreement with the trend of $\Sigma\text{PAH}/\text{TIR}$ versus metallicity measured in other samples. In higher metallicity star-forming galaxies, $\Sigma\text{PAH}/\text{TIR} \sim 10 - 20\%$ [10] but declines to a range of 0.1 – 1.6% in lower metallicity galaxies [34]. Our Sextans A measurements extends this correlation to $\Sigma\text{PAH}/\text{TIR} = 0.15\%$ at 7% Solar metallicities, the lowest metallicity detection to date.

The difference in spatial resolution between the FIR data ($\sim 30''$) and the PAH clumps ($\sim 1''$) makes it difficult to determine $\Sigma\text{PAH}/\text{TIR}$ at the scale of the PAH clumps. If the overall dust distribution is less concentrated than the PAH emission on these small scales, the resulting $\Sigma\text{PAH}/\text{TIR}$ would likely be higher in the clumps. To test whether the PAHs are more compact than the overall dust distribution, we use the F1500W filter as a proxy for the stochastically heated small dust grain population since F2100W

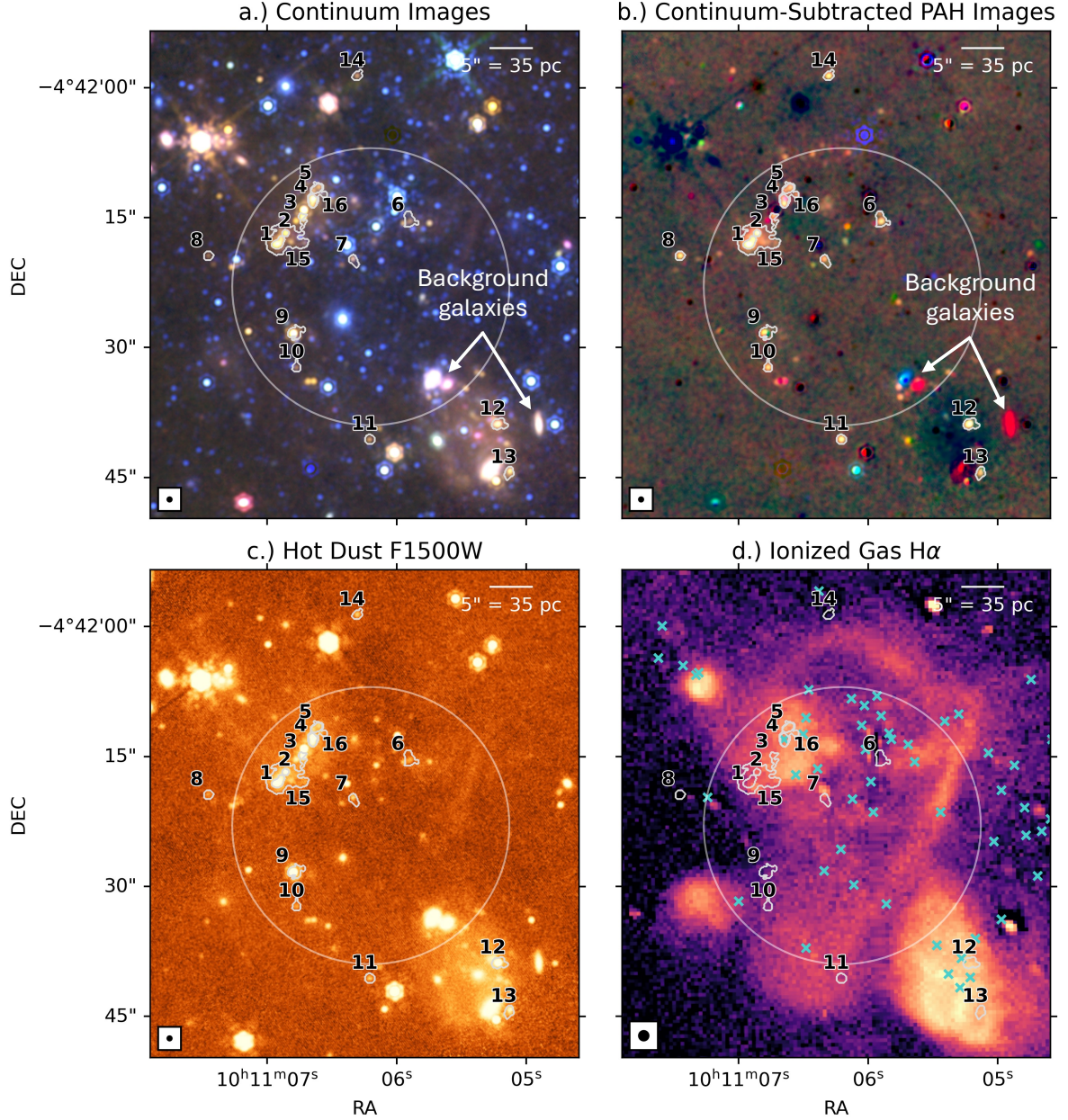


Fig. 3 PAH emission clumps and their spatial distribution in Sextans A Clump structures and labels defined with the dendrogram structure analysis (see Section 3.3) overlaid on Sextans A JWST and $H\alpha$ data. Clump properties are described in Table 1. We require a 3σ detection in all three PAH bands— 3.3, 7.7, and $11.3\ \mu\text{m}$ — to define a PAH emission clump. We present the clumps on: a.) RGB 3-color images of the stellar and hot dust continuum and b.) the continuum-subtracted PAH flux in each PAH band, where the red color is $11.3\ \mu\text{m}$, green is $7.7\ \mu\text{m}$, and blue is $3.3\ \mu\text{m}$ all scaled at the same *asinh* stretch to emphasize extended emission. Emission from continuum dominates in Sextans A, as there are many more features in the continuum image as compared to the PAH data. The continuum-subtracted PAH data show the importance of requiring a detection in all three PAH bands, as spurious background galaxies can be bright in a single band, resulting in the red and blue artifacts in the PAH RGB image. PAH clumps are visible as the yellow and white clumps of emission outlined from the PAH clump boundary. The white circle marks the “sf-3” region defined in Shi et al. [67] used to calculate the total infrared luminosity and compare to the PAH flux. c.) Observations of the F1500W filter, which acts as a high resolution probe of the hot dust as the reddest available filter in our JWST dataset. PAH clumps frequently appear near regions of hot dust, though the hot dust exhibits a more extended spatial distribution, especially in the southern region near clumps 12 and 13. d.) $H\alpha$ observations of Sextans A from Kennicutt et al. [72] that trace the ionized gas, which shows similar spatial distribution with the F1500W hot dust map. We also overlay the massive star catalog from Lorenzo et al. [73], including O and early-type B stars, as the cyan “x” symbols. Some PAH clumps are spatially coincident with regions of $H\alpha$ emission, though they generally do not coincide with the brightest $H\alpha$ peaks, suggesting a complex geometry between the photodissociation region (PDR) and HII region structure.

Table 1 Clump Properties

Clump	RA (10h 11m s)	Dec. (-04° 42' ")	Radius (pc)	Major Axis (pc)	Minor Axis (pc)	3.3 μ m Flux (μ Jy)	7.7 μ m Flux (μ Jy)	11.3 μ m Flux (μ Jy)
1	06.915	17.993	1.97	2.58	1.50	1.70 ± 0.04	5.69 ± 0.06	14.15 ± 0.20
2	06.857	16.798	1.20	1.22	1.18	0.53 ± 0.02	1.24 ± 0.02	4.38 ± 0.10
3	06.727	15.057	1.99	2.96	1.33	0.13 ± 0.01	0.39 ± 0.02	1.70 ± 0.05
4	06.648	13.163	1.81	2.33	1.41	0.83 ± 0.02	1.22 ± 0.02	6.84 ± 0.11
5	06.612	11.647	1.72	2.26	1.31	0.31 ± 0.01	0.76 ± 0.02	2.33 ± 0.05
6	05.898	15.334	2.17	2.57	1.84	0.38 ± 0.02	1.08 ± 0.03	2.51 ± 0.06
7	06.332	19.912	1.71	2.24	1.30	0.10 ± 0.01	0.50 ± 0.02	1.28 ± 0.04
8	07.451	19.418	1.40	1.44	1.36	0.17 ± 0.01	0.76 ± 0.02	1.82 ± 0.05
9	06.790	28.257	2.09	2.53	1.74	0.27 ± 0.02	1.28 ± 0.03	3.45 ± 0.08
10	06.771	32.283	1.44	1.59	1.31	0.13 ± 0.01	0.63 ± 0.02	1.78 ± 0.05
11	06.206	40.610	1.43	1.44	1.42	0.30 ± 0.01	1.03 ± 0.02	2.66 ± 0.06
12	05.217	38.846	1.73	1.97	1.52	0.76 ± 0.02	2.32 ± 0.04	4.57 ± 0.10
13	05.131	44.443	1.69	2.06	1.38	0.19 ± 0.01	0.72 ± 0.02	1.06 ± 0.04
14	06.303	58.643	1.45	1.61	1.30	0.22 ± 0.01	0.89 ± 0.02	2.15 ± 0.05
15 [†]	06.888	17.685	4.87	6.02	3.94	3.83 ± 0.06	11.43 ± 0.09	32.89 ± 0.26
16 [‡]	06.629	12.532	3.64	5.61	2.37	1.28 ± 0.03	2.34 ± 0.04	10.56 ± 0.13

[†] Clump 15 is a larger structure that encompasses clumps 1 and 2

[‡] Clump 16 is a larger structure that encompasses clumps 4 and 5

Table Notes: The properties of the PAH clumps defined through dendrogram structure analysis, using the continuum-subtracted 7.7 μ m data to calculate the center and size of the clumps. The centers of the clumps are reported in right ascension and declination in columns 2 and 3. The deconvolved radius, major axis, and minor axis of each clump are reported in columns 4 through 6. The continuum-subtracted flux for the 3.3 μ m, 7.7 μ m, and 11.3 μ m PAH features are reported in columns 7 through 9.

is not available to calculate R_{PAH} [76, 89–91]. While F1500W does contain some PAH emission from the wings of the fainter 12.8, 13.6, 14.8, and 16.4 features [7], as our reddest filter, it is the best probe of the stochastically heated hot dust distribution that has matched resolution to the PAH emission. We use the same TIR area defined in Shi et al. [67], which is similar to the FIR beam size (32"), and require a similar 3σ pixel cutoff to sum the emission in the F1500W filter. We measure $\Sigma\text{PAH}/\text{F1500W} = 0.36$ for the region. We then compare $\Sigma\text{PAH}/\text{F1500W}$ for the individual PAH clumps and find that every PAH clump except clump 9 has a $\Sigma\text{PAH}/\text{F1500W}$ greater than the value across the TIR region. We calculate an average of $\Sigma\text{PAH}/\text{F1500W} = 0.76$, with a range of $\Sigma\text{PAH}/\text{F1500W} = 0.17 - 2.5$, much larger than the value for the 32" circle. We interpret the difference in $\Sigma\text{PAH}/\text{F1500W}$ measured over the FIR beam versus the PAH clumps as evidence that PAHs are confined to the small clumps, while non-PAH small grains reside in a more extended distribution. This matches the visual appearance of the JWST maps (see Figures 3 and 4), the SED analysis of the emission, and the analysis of a clump radial profile (see Section 3.5). Given that the spatial distribution of cold dust emitting in the FIR is expected to be even more extended than the dust traced by 15 μ m emission, the $\Sigma\text{PAH}/\text{TIR}$ measured for Sextans A within the FIR beam is likely significantly lower than it would be if it could be estimated on the small scale of PAH clumps. This suggests that the PAH deficit at low metallicity may be partially driven by the small filling factor of PAHs relative to the more extended dust distribution, though it is not the only effect driving the low PAH abundance. The previous Spitzer-based measurements in Figure 5 probe much larger physical scales (~ 500 pc or more), meaning that any such PAH beam dilution effect would have been unresolved in earlier studies.

Theoretical models and laboratory experiments indicate that the relative PAH feature strengths depend on the PAH grain size, ionization state, and the incident radiation field. [92–96]. We can estimate the properties of the PAH grains at this very low metallicity with the photometry of the 3.3 μ m, 7.7 μ m, and 11.3 μ m features studied in this work. As the shortest wavelength feature, the 3.3 μ m band is most sensitive to the smallest PAHs, which can be heated by the absorption of a single photon to temperatures hot enough to emit at the shorter infrared wavelengths [96, 97]. Laboratory data also show that the 3.3 and 11.3 μ m features originate from predominantly neutral PAHs [7, 98]. Therefore, the 3.3 μ m/11.3 μ m ratio serves as an effective tracer of PAH size distribution. In contrast, the 7.7 μ m feature is associated with charged PAHs and the 7.7 μ m/3.3 μ m ratio probes the degree of ionization in the PAH population [92].

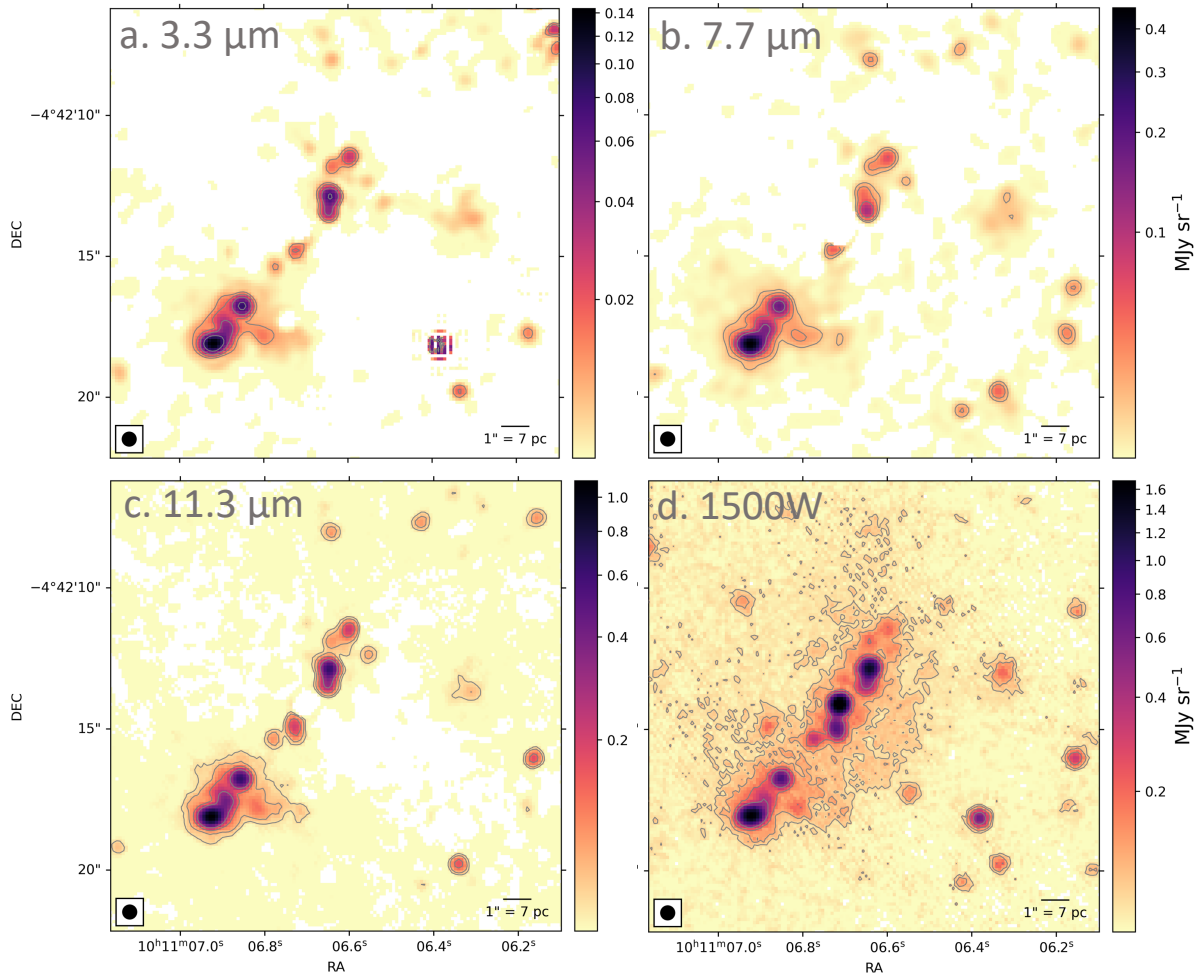


Fig. 4 Continuum-subtracted images of the 3.3, 7.7, and 11.3 μm features reveal compact and clump structure The PAH emission flux for the three PAH features, as well as the hot dust from the F1500W filter, targeted through the photometric imaging in JWST GO 2391. The region is defined by the green square in Figure 1 and is the area with the brightest and most concentrated PAH emission. All data is PSF matched to the F1500W filter prior to continuum subtraction, ensuring each image has a resolution of $\sim 0.48''$ (PSF in bottom left corners). PAH emission clumps are compact, comparable to the PSF, with sizes of $0.5 - 1.5''$ or $3 - 10$ pc. Contours are at the 3σ , 5σ , 10σ , and 20σ level.

The comparison between the $3.3 \mu\text{m}/7.7 \mu\text{m}$ and $3.3 \mu\text{m}/11.3 \mu\text{m}$ ratios from the D21 model grids and the PAH clumps observed in Sextans A is presented in Figure 6 (see Section 3.6 for details). Overall, the $3.3 \mu\text{m}/11.3 \mu\text{m}$ band ratios from the PAH clumps tend to agree with the “small” and “standard” D21 size distributions, but there is scatter across the clumps. The $3.3 \mu\text{m}/7.7 \mu\text{m}$ band ratios for nearly all the clumps are inconsistent with the D21 ionization grids, suggesting that the PAHs in Sextans A are more neutral than the “low ionization” grid used in the D21 models². The preference for smaller, more neutral PAHs is similar to other studies that target low metallicity regions, including the SMC [43], M101 [38, 59], II Zw 40 [58, 106], and 30 Doradus in the LMC [107]. We also plot in red triangles results from the PDRs4All spectra from the Orion Bar PDR [102–105] that, for consistency, follow the same continuum subtraction procedure as the PAH clumps in Sextans A. In contrast to Sextans A, the PDRs4All spectra are in agreement with both the ionization and size grid from the D21 models, suggesting that the elevated $3.3 \mu\text{m}/7.7 \mu\text{m}$ ratio in Sextans A is significant and not due to inconsistencies with the continuum subtraction.

The Sextans A PAH clumps in Figure 6 are colored by $\text{H}\alpha$ data from the Local Volume Legacy (LVL) survey [72, 99] to provide an estimate of the ionizing radiation. There is a moderate correlation between

²The treatment of charge state of PAHs in the D21 models may also not capture the complexity of the PAHs in Sextans A, as the models do not distinguish among the PAH ionization states (e.g., anions, cations, dications) and do not allow for variations in aliphatic/aromatic fraction or other structural characteristics.

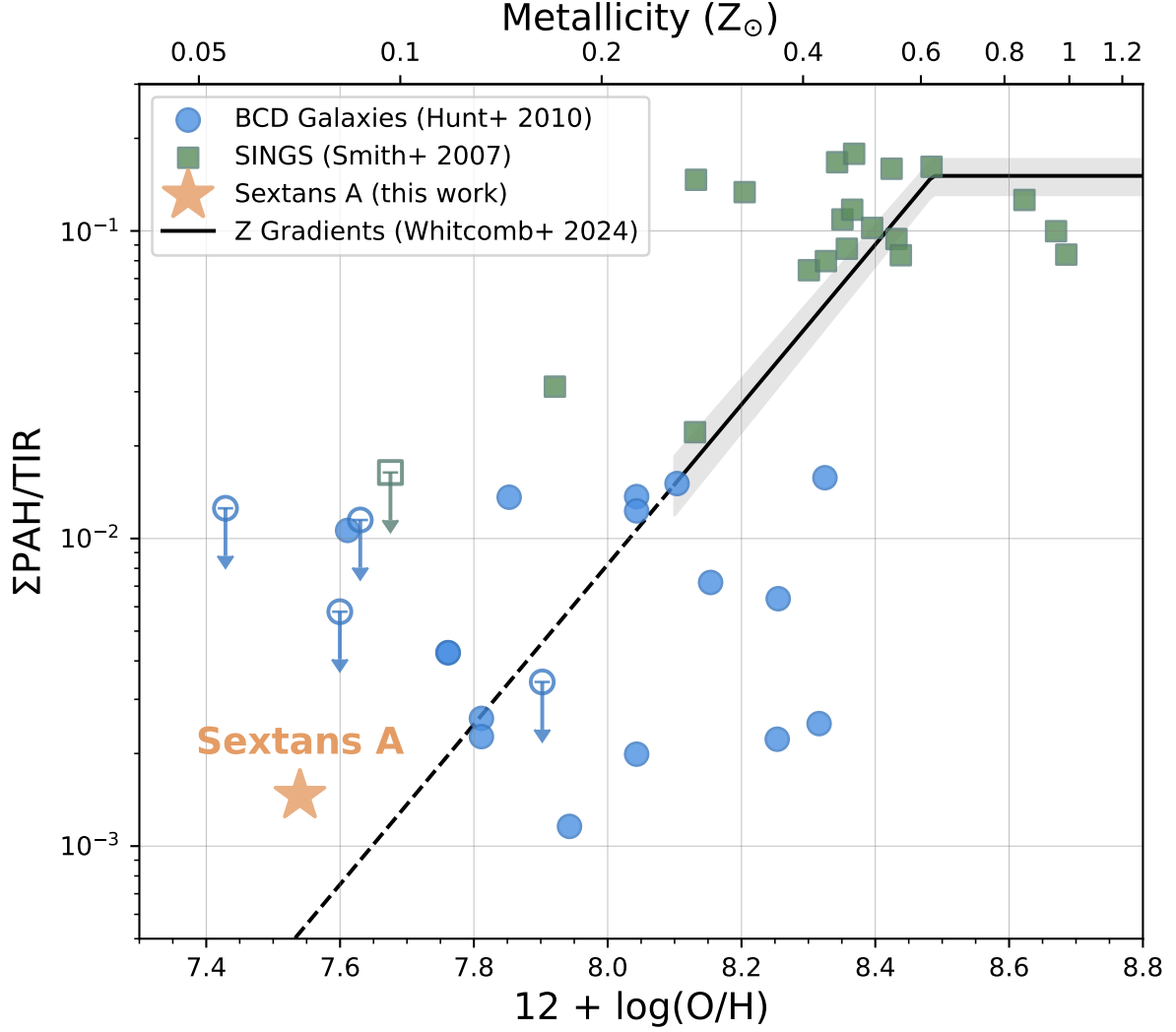


Fig. 5 The fraction of infrared power emitted by PAH features as a function of metallicity Comparison of $\Sigma\text{PAH}/\text{TIR}$, the ratio between the integrated intensity of detected PAH features and the total infrared luminosity, across a range of galaxy samples. Sextans A is shown as the orange star, the sample of metal-poor blue compact dwarf (BCD) galaxies from Hunt et al. [34] are displayed as blue circles, and the higher metallicity non-AGN SINGS galaxies from Smith et al. [10] are the green squares. We also plot the empirical fit of $\Sigma\text{PAH}/\text{TIR}$ as a function of the metallicity gradients for the galaxies M101, NGC 628, and NGC 2403 from Whitcomb et al. [38] in the black line, with the uncertainty presented as gray bars and the extrapolation shown as the dashed line. Sextans A is the lowest metallicity galaxy with a robust detection of PAH emission and generally $\Sigma\text{PAH}/\text{TIR}$ follows the trends with metallicity seen in the other samples. Figure adapted from Hunt et al. [34].

the $3.3\,\mu\text{m}/11.3\,\mu\text{m}$ (grain size) and $3.3\,\mu\text{m}/7.7\,\mu\text{m}$ (ionization) ratios and the $\text{H}\alpha$ flux, with Spearman rank coefficients of $r_{sp} = 0.61$ and $r_{sp} = 0.68$, respectively³. However, there is no correlation between the $\text{H}\alpha$ flux and the $7.7/11.3$ (ionization) ratio ($r_{sp} = -0.19$). We also test the correlation with *Swift* UVOT W1 data to trace the UV radiation field and find the same trends, with comparable Spearman rank correlation coefficients ($r_{sp} \sim 0.6$), indicating that the results are robust to the choice of radiation field tracer.

The increasing $3.3\,\mu\text{m}/11.3\,\mu\text{m}$ ratio with ionizing flux is opposite to what one might expect, as a common interpretation for the PAH deficit at low metallicity is enhanced photodestruction of smaller PAHs in strong UV radiation fields [26, 28, 32, 34, 109]. Because the smallest PAHs are the most easily destroyed [40, 41], one would anticipate lower $3.3\,\mu\text{m}/11.3\,\mu\text{m}$ or $3.3\,\mu\text{m}/7.7\,\mu\text{m}$ ratios in regions with

³The correlation persists when using the ionized gas fraction, defined as $\text{H}\alpha$ flux normalized by the 21 cm atomic gas emission [108]. Due to the coarse resolution of the 21 cm data, only the $\text{H}\alpha$ based coefficients are reported.

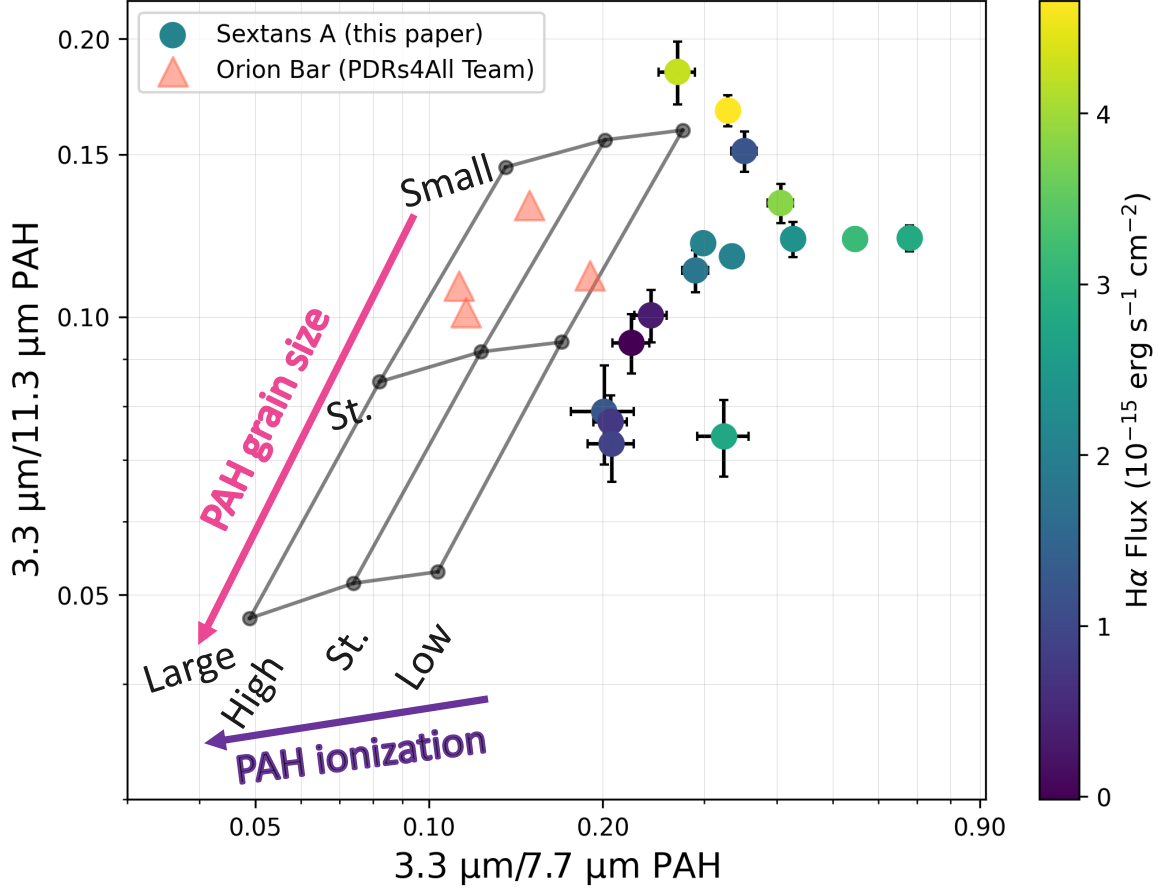


Fig. 6 Ratios between PAH features in Sextans A Band ratios for the PAH emission clumps defined in Table 1, using the continuum-subtracted fluxes for the 3.3, 7.7, and 11.3 μm features. The points are colored by the $\text{H}\alpha$ flux from the LVL survey [88, 99] and show a correlation ($r_{\text{sp}} \sim 0.6$) between the $\text{H}\alpha$ flux and the $3.3\mu\text{m}/11.3\mu\text{m}$ and $3.3/7.3$ ratios. We overlay model predictions from D21 with the low metallicity $Z = 0.0004 \approx 0.02Z_{\odot}$, 10 Myr star burst from Bruzual and Charlot [100] as the input spectrum and average the results for radiation field intensities of $U = 0 - 3.5$ since there is little scatter. The model grids show band ratio predictions for the size of PAHs, ranging from small ($a_{01} = 3\text{\AA}$) to large ($a_{01} = 5\text{\AA}$) size distributions, and the ionization of the PAHs, with standard (St.) values corresponding to the ionization fraction given in Draine and Li [101]. Red triangles are spectroscopy from the Orion Bar [102–105] where we applied synthetic photometry and the same continuum subtraction as the Sextans A PAH clumps to provide a direct comparison. Overall, the $3.3\mu\text{m}/11.3\mu\text{m}$ band ratio suggests that the PAHs in Sextans A are more similar to the small and standard size distributions assumed in D21. The ionization grids, however, are inconsistent with the Sextans A band ratios, suggesting that the PAHs in Sextans A are more neutral than models assume.

stronger radiation fields. Instead, the positive correlation between these ratios and UV radiation field strength suggests enhancement of the $3.3\mu\text{m}$ feature. Rather than attributing this trend to changes in the PAH grain size distribution, we propose that the $3.3\mu\text{m}$ feature is particularly sensitive to the hardness of the radiation field (see Figure 16 in D21). As the radiation field becomes harder, the $3.3\mu\text{m}$ flux relative to the TIR increases more rapidly than any other PAH feature. There is also a similar effect at very high intensity radiation fields ($U > 10^4$) where the $3.3\mu\text{m}$ PAH flux increases relative to the 11.3 and $7.7\mu\text{m}$ features. Since the $\text{H}\alpha$ and *Swift* UVOT W1 data will trace a combination of both the hardness and the intensity of the incident radiation field, it is difficult to determine which effect is driving this correlation, but we note that the higher radiation field intensities ($\log U > 10^4$) are not preferred after fitting the observed SEDs (see Section 3.4), suggesting that the hardness of the radiation field may contribute to the correlation more.

The lack of evidence of significant processing by the ionizing radiation in Sextans A contradicts the hypothesis that the PAH deficit at low metallicity is driven solely by enhanced radiation fields destroying PAHs. Instead, our observations favor inhibited PAH grain growth as the origin of the low PAH abundances in Sextans A. This interpretation aligns with the framework introduced by Whitcomb

et al. [38], based on *Spitzer* spectroscopy of metallicity gradients in M101, NGC 628, and NGC 2403 ($0.25 - 1.0 Z_{\odot}$, see Figure 5), which revealed that PAH feature power shifts to shorter wavelengths as metallicity decreases (e.g., enhanced $3.3 \mu\text{m}$ relative to $11.3 \mu\text{m}$), implying smaller PAH grain size distributions. As the lowest metallicity galaxy with detected PAH emission to date, Sextans A provides a critical test of the inhibited grain growth prediction for the $3.3 \mu\text{m}$ PAH fraction ($\text{PAH } 3.3 / \Sigma\text{PAH}$) at $\lesssim 10\% Z_{\odot}$. We derive an upper limit of $\text{PAH } 3.3 / \Sigma\text{PAH} \lesssim 7.7\%$, consistent with the $6.3 - 9.7\%$ range predicted in the inhibited PAH grain growth model in Whitcomb et al. [59].

The ionization state and spatial distribution of PAH emission in Sextans A also provides a key new observational constraint for understanding the behavior of these important grains at low metallicities. Figure 6 shows that the $7.7 \mu\text{m}$ feature is under-luminous compared to the D21 models, suggesting that the PAH population in Sextans A may be more neutral than those models assume. The PAH ionization state is governed by the balance between photoionization and recombination with electrons and ions in the gas, and can be parameterized as $U\sqrt{T_e}/n_e$ [69]. Cooler temperatures, higher densities, and weaker radiation fields therefore favor a more neutral PAH population. The faint $7.7 \mu\text{m}$ feature implies that the PAHs reside in dense, cold, and shielded regions of the ISM, consistent with the compact morphology ($0.5 - 1.5''$ or $3 - 10 \text{ pc}$) of the resolved PAH clumps (see Figure 4) and provide an ideal environment for the formation and survival of molecules.

We therefore suggest that these dense, shielded clumps of PAH emission in Sextans A represent active sites of PAH growth in the ISM. This interpretation is supported by increasing evidence that PAHs and their aromatic precursors form within molecular clouds [110–114] and that extinction curve variations in the Milky Way are driven by PAH growth [115]. In Sextans A, the preference for a small PAH grain size distribution and the agreement with the inhibited PAH grain growth model, combined with the lack of evidence for significant processing by radiation fields, suggests that the PAHs were created in-situ rather than formed elsewhere. The concentration of PAHs in well-shielded clumps supports formation in these dense regions, with PAH nanoparticles surviving only a finite time in more diffuse environments outside of the clumps [35, 40, 41, 43, 116–118]. Furthermore, since the PAH growth timescale scales roughly with density and inversely with metallicity, growth in Sextans A is expected to proceed at least 30 times more slowly than at Solar metallicity and requires dense regions. This extended timescale naturally suppresses the formation of large PAHs, consistent with the small-grain size distribution observed in the clumps.

In metal-poor systems with more extreme conditions than Sextans A, the balance between PAH production and destruction mechanisms can shift. For example, Hunt et al. [34] report *Spitzer* spectroscopy of Blue Compact Dwarf (BCD) galaxies, which typically have higher radiation field intensities than Sextans A, and propose that the PAH deficit at low metallicity is driven by photodestruction rather than inhibited growth. Further, Lai et al. [58] presents JWST spectroscopy of the BCD galaxy II Zw 40 and find a bright $3.3 \mu\text{m}$ feature relative to other PAH bands, consistent with the inhibited PAH grain growth model, but also an anti-correlation between the $3.3 \mu\text{m}/11.3 \mu\text{m}$ ratio and radiation field hardness, indicating that the PAH size distribution at low metallicity is governed by the interplay between photodestruction and inhibited growth. Future observations of BCD galaxies targeting the $3.3 \mu\text{m}$ feature will be essential, as the $3.3 \mu\text{m}/11.3 \mu\text{m}$ ratio provides the most sensitive diagnostic of PAH size [98]. Along with Sextans A, these results together suggest that the driver of the PAH deficit at low metallicity depends on the local physical conditions of a given galaxy.

The detection of PAHs in Sextans A has far-reaching implications for future observations of both nearby and high-redshift galaxies. Since PAHs can survive and form in a 7% Solar metallicity environment, they will play important roles in ISM physics in galaxies out to high redshift where average metallicities are much lower than Solar [e.g. 12, 14, 48–50]. We favor the interpretation that the PAH deficit at low metallicity is caused by inhibited PAH grain growth and find evidence that PAHs form in-situ in the ISM in the compact clumps in Sextans A. This implies that the PAH lifecycle is governed by the balance between grain growth and shielding from radiation fields, processes that will shape PAH emission in both nearby and high-redshift galaxies.

3 Methods

3.1 JWST Data and Processing

The JWST [119, 120] observations of Sextans A (GO 02391, PI: J. Roman-Duval) targeted the brightest, most active star-forming region with a far-infrared dust detection [67]. The observations consist of NIRCam [121, 122] and MIRI [123, 124] broadband imaging focused on the filters that isolate the 3.3 μm (NIRCam F335M), 7.7 μm (MIRI F770W), and 11.3 μm (MIRI F1130W) PAH features, as well as filters that bracket each PAH filter to estimate and subtract hot dust and stellar continuum that can overwhelm faint emission. A single MIRI pointing covers the star-forming region that overlaps with Module B of the NIRCam pointing. Figure 1 presents the data and shows the location of the MIRI and NIRCam coverage on Sextans A.

3.1.1 Observations and Data Reduction

The NIRCam observations of Sextans A were taken on January 2nd, 2023 and consist of six NIRCam Imaging filters: F115W, F150W, and F200W for the short wavelength detectors and F300M, F335M, and F360M for the long wavelength detectors. The F150W/F300M and F115W/F360M filter combination contained 8 total integrations, with 4 dithers in the INTRAMODULEX pattern, and 5 groups per integration using a MEDIUM8 readout pattern leading to a total integration time of 4166 s. The F200W/F335M filter combination was similar, but used 10 groups per integration to obtain a deeper exposure of 8561 s with the PAH filter, F335M. The majority of the MIRI Imaging data was taken on January 2nd and 4th, 2023, including the filters F560W, F770W, F1000W, and F1500W. JWST observed Sextans A with the F1130W filter 4 months later, on April 13, 2023, which results in a different orientation with respect to North when compared to the other observations. All of the MIRI observations use the FASTR1 readout pattern, 4 dithers in the 4-Point-Sets optimized for extended emission, but vary on the integrations per exposure as follows: 7 integrations per exposure for F560W (7837 s integration time), 8 integrations per exposure for F770W (8958 s integration time), 25 integrations per exposure for F1000W (28016 s integration time), and 30 integrations per exposure for both F1130W and F1500W (33622 s integration time). The exposure time for each filter was calculated through the Exposure Time Calculator [ETC; 125] to account for the increase in noise as a function of wavelength due to the JWST backgrounds.

The NIRCam and MIRI data are reduced with version 1.15.1 (DMS build B11.0rc2) of the JWST Science Calibration Pipeline [126] and CRDS context `jwst_1263.pmap` [127] through all three stages of the pipeline. For NIRCam, we follow the default parameters, except in stage one where we allow the frame0 correction to recover stars that saturate in the first group (`suppress_one_group = False`) for the ramp step and we apply the correction for snowballs (`expand_large_events = True`) in the jump step. In between stage two and three, we corrected the $1/f$ noise that manifests as striping in the NIRCam filters with the algorithm presented in Willott et al. [128]. For alignment in stage three, we use a catalog of point sources from HST PID 16104 (PI: J. Roman-Duval) which are aligned to GAIA DR3 to obtain a high quality absolute astrometric solution. We modify the tweakreg parameters to have a SNR threshold of 5 and a tolerance of 0.1 for the short wave detectors to improve the alignment. For MIRI, we follow mostly default parameters, except in stage one we slightly increase the cosmic ray rejection threshold from 4 to 5 sigma in the jump step. A high quality alignment in MIRI is more difficult to achieve due to the lack of point sources at longer wavelengths. We therefore take advantage of the excellent relative astrometry for a given visit when using the same guide star [120]. First, we align the F560W mosaic to the HST PID 16104 source catalog because F560W will contain the most point sources compared to the longer wavelength MIRI filters. Then, we use the astrometric solutions for F560W and apply them to F770W, F1000W, and F1500W which were all taken within the same day and use the same guide star. For F1130W, which was observed four months later, we create a point source catalog from the F1000W filter to align the F1130W mosaic. The final resulting mosaics have high quality alignments that are well matched from the NIRCam to MIRI filters.

3.1.2 Background Subtraction

The MIRI imaging sensitivity is background limited [123] and the imaging of Sextans A is dominated by the background from zodiacal light and the thermal background of the telescope. While dedicated

background observations in conjunction with MIRI imaging are usually taken to remove the background component, the large integration time required for detecting faint PAHs in Sextans A made dedicated background observations prohibitive. Instead, we create a background from the data itself by stacking the four dithered exposures used to create each mosaic. The four exposures are stacked together in detector coordinates and sources from the image are removed by sigma clipping and taking the median value for each pixel. The 4-point extended source dither pattern maximizes the dither size to about $20''$, which is 18 – 27% of the size of the MIRI imager. These large dither sizes enable efficient sigma clipping of the sources in Sextans A, including point sources and diffuse emission on the scale of $20''$ or less. We iteratively remove pixels that are three times the standard deviation of a given image pixel. All the structure from the JWST images of Sextans A is therefore removed, leaving only the background from the MIRI imaging detector. We note that it is possible that faint, extended emission larger than $20''$ may be subtracted out of the Sextans A mosaics. Given that the largest structure in the NIRCcam imaging is $< 10''$ in size, it is unlikely that the MIRI background subtraction method is missing emission.

The NIRCcam detector sensitivity is not background limited, but does contain a contribution from the background that is wavelength dependent and should be removed in order to compare to the background subtracted MIRI data and for continuum subtracting the PAH emission. We calculate the NIRCcam background in a similar fashion to the MIRI background through stacking the four dithered exposures in detector coordinates and sigma clipping as many sources as possible. The dither pattern in NIRCcam, however, is much more compact and leads to a few arcsecond differences between the images, which is not large enough to exclude astronomical sources. Instead, we sigma clip out as many sources as possible and fit the resulting image with a smoothly varying two-dimensional first order polynomial to mimic the zodiacal light background that dominates at these wavelengths. We compare both the MIRI and NIRCcam background estimates to the JWST background tool [129] and find excellent agreement.

3.1.3 PSF Matching JWST data to a common resolution

The size of the JWST point spread function (PSF) increases as a function of wavelength and changes substantially between data taken with NIRCcam and MIRI. The PSF of images taken in each filter therefore needs to be carefully matched across filters in order to subtract the continuum estimated from bracketing filters from the PAH filters. We also compare the $3.3\ \mu\text{m}$, $7.7\ \mu\text{m}$, and $11.3\ \mu\text{m}$ continuum subtracted PAH emission, which necessitates having the same PSF for all filters. We use the procedure outlined in Aniano et al. [130] to create convolution kernels that transform an image with a narrower PSF to a broader PSF. The PSFs used to create the convolution kernels are taken from STPSF/WebbPSF version 1.3.0 [131], which generates PSF models informed by in-flight wavefront sensing measurements. Since JWST Cycle 1, these models have been updated to incorporate detector effects and match the observed empirical PSFs very well [e.g., 132]. The short wavelength NIRCcam filters (F115W, F150W, and F200W) are not PSF matched because they are not used in the PAH continuum subtraction procedure. The narrowest PSF we use is for the F300M filter, which has a full width half max (FWHM) of $0.''097$, and the largest PSF is for the F1500W filter, which has a FWHM of $0.''488$. We create custom convolution kernels that match the long wavelength NIRCcam filter PSFs (F300M, F335M, F360M) and the MIRI filter PSFs (F560W, F770W, F1000W, F1130W) to the F1500W PSF, as it is the widest. We do not circularize the PSFs as suggested in Aniano et al. [130], because the JWST PSF is highly structured and asymmetrical, and we therefore produce much higher quality kernels without circularization. The PSFs are rotated to the orientation angle of each mosaic. This is especially important for filter F1130W, which was observed a few months later than the rest of the data, resulting in the PSF spikes in the native image being rotated compared to the other filters.

We convolve the images to the PSF of the F1500W filter with the custom kernel created for each filter. We then regrid the mosaics to the F1500W coordinate system. These images are used for all analysis and have a PSF of $0.''488$. This resolution element corresponds to 3.3 pc when assuming a distance of 1.4 Mpc for Sextans A [62, 63].

3.1.4 Continuum Subtraction of the PAH filters

The near- and mid-infrared spectra of nearby galaxies are complex, comprised of broad PAH emission features, continuum from both starlight and stochastically heated small dust grains, as well as bright ionized gas emission lines. Although spectroscopic observations are most effective for isolating PAH

features and removing the underlying continuum, the $\sim 5''$ field of view and limited sensitivity of the JWST spectroscopic instruments make observations of star-forming regions in nearby dwarf galaxies prohibitive. In this work, we instead use photometric observations that flank the PAH bands on both the red and blue sides to constrain the continuum slope, allowing an estimate of the underlying continuum emission in the PAH-centered filters. However, the near- and mid-infrared spectrum hosts a rich set of PAH features spanning 3–20 μm [e.g., 7, 69], so even filters chosen to trace the continuum include some PAH emission (see Figure 7). Several approaches have focused on continuum subtraction of the F335M filter by accounting for PAH emission in the flanking F360M filter [59, 71, 106, 133, 134] and empirical calibrations have also been developed for the MIRI F770W and F1130W filters [134, 135]. Building upon this work, we generalize the continuum subtraction procedure to all filters centered on PAH emission—F335M, F770W, and F1130W. Our method is compatible with the approach outlined in Sandstrom et al. [71] and Whitcomb et al. [59] for the F335M filter, but flexible enough to account for the broader and brighter PAH features probed by MIRI (see Figure 7). We outline our assumptions and describe the method below.

Within each filter trio, we assume the following: one filter is centered on and dominated by PAH emission, a second primarily traces the continuum but includes some contamination from nearby PAH complexes, and a third provides a clean measure of the continuum with no PAH contribution. For the F300M/F335M/F360M trio, we take F300M as the clean continuum filter and F360M as the PAH-contaminated flanking filter, affected by the 3.4 and 3.47 μm plateaus of aromatic and aliphatic features [106, 136, 137]. In the mid-infrared, we assume F1000W is not heavily contaminated by PAH emission. By contrast, F560W is affected by the 5.2, 5.6, and 6.2 μm features and F1500W is contaminated by the wings of the 12.8, 13.6, 14.8, and 16.4 μm features. To illustrate the filter coverage, Figure 7 shows the transmission curves overlaid on both a model PAH spectrum [69] and an empirical spectrum of the PDRs4All Orion Bar JWST/NIRSpec and MIRI/MRS observations [102–105]. We apply synthetic photometry to both spectra, highlighting which PAH features are traced by each filter, and present the PAH-centered filters in green, the flanking filter with PAH contamination in gold, and the clean continuum filters in magenta.

Next, we assume that the level of PAH contamination in the flanking filter scales linearly with the brightness in the main PAH filter. While the brightness of each PAH feature does depend on the size and ionization of the grains, we account for this by varying the size and charge distribution from D21 models and propagate this uncertainty throughout. Lastly, we assume the slope of the continuum can be approximated as linear between the two filters that flank the PAH emission.

With those assumptions, we then define each filter as:

$$\begin{aligned} f_1 &= f_{c1} \\ f_2 &= f_{c2} + f_{p2} \\ f_3 &= f_{c3} + f_{p3}. \end{aligned} \tag{1}$$

Here, f_1 is the flux of the filter with only continuum emission. f_2 is the flux of the filter centered on the PAH emission and contains contributions from both continuum (f_{c2}) and PAH flux (f_{p2}). Lastly, f_3 is the flux from the filter that is contaminated by adjacent PAH features and therefore contains contributions from both continuum (f_{c3}) and PAH emission (f_{p3}). We then assume that the PAH emission in the central PAH filter scales linearly (through a proportionality constant k) with the contaminating PAH emission in the adjacent continuum filter.

$$f_{p2} = k f_{p3}. \tag{2}$$

With small wavelength differentials ($< 5\mu\text{m}$), we assume that the slope of the continuum between f_1 and f_3 is linear and calculate the continuum in f_2 :

$$f_{c2} = \frac{f_{c3} - f_{c1}}{\lambda_3 - \lambda_1} \times (\lambda_2 - \lambda_1) + f_{c1} \tag{3}$$

where λ is the pivot wavelength of a given filter. We define:

$$\beta = \frac{\lambda_2 - \lambda_1}{\lambda_3 - \lambda_1} \tag{4}$$

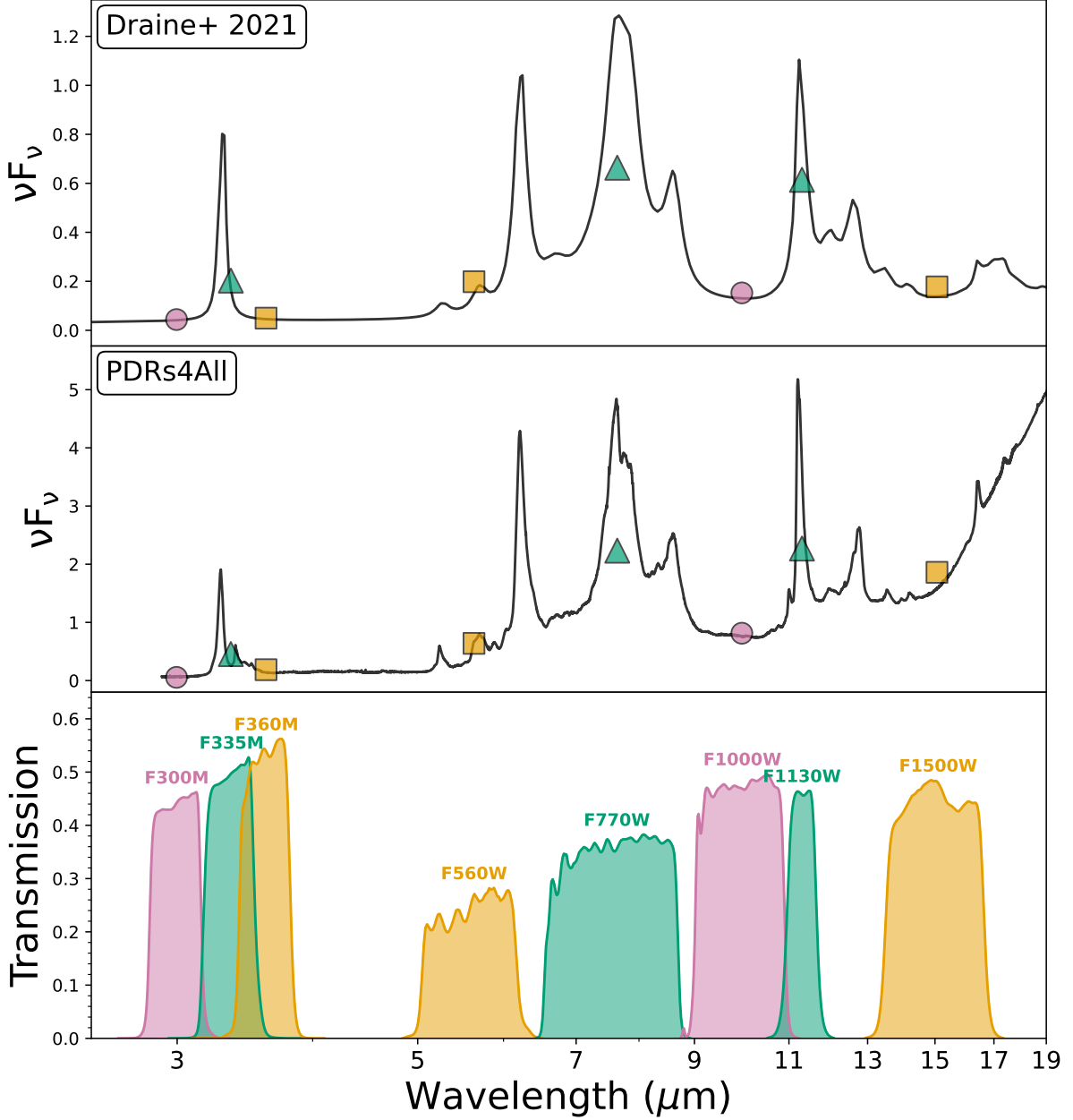


Fig. 7 Filters and spectral templates used for PAH continuum subtraction JWST filter transmission curves used for the PAH continuum subtraction in this work (bottom panel) and two example mid-infrared spectra that show the PAH features in arbitrary flux units. The top panel is a model from [D21](#) ($\log U = 1$; standard size and ionization distributions) and the middle panel is empirical data from PDRs4All with lines removed (dissociation front 1 template spectrum) [[102–105](#)]. The wavelength coverage of each filter shows which PAH features are contained in a given filter and are color coded by whether they are defined as the main PAH filter (green and triangle; F335M, F770W, and F1130W), the continuum filter without substantial PAH contamination (gold and square; F360M, F560W, and F1500W), or the continuum filter that is contaminated by PAH complexes (magenta and circle; F300M and F1000W). These filters are used in conjunction to calculate the continuum subtracted PAH flux in the main PAH filter (see Section [3.1.4](#) and Equation [1](#)). We also apply synthetic photometry for each filter on the two example spectra.

to simplify the resulting equations. By combining equations [1](#), [2](#), [3](#), and [4](#), we calculate f_{p2} , the continuum subtracted PAH flux in the main PAH filter for a given k :

$$f_{p2} = \frac{k}{k - \beta} \times [f_2 - (1 - \beta)f_1 - \beta f_3], \quad (5)$$

which is the same functional form as Equation 1 in Whitcomb et al. [59] for direct comparison.

Estimating the PAH flux in filter 2, f_{p2} , relies on a value for k , the degree of PAH emission contaminating the flanking filter. We determine k through a combination of the D21 PAH models and empirical JWST spectra from the PDRs4All program [102–105]. We summarize our procedure to calculate k as follows. First, we separate the PAH features from the underlying continuum emission in the spectrum. Then, we compute synthetic photometry for only the PAH portion of the spectrum, calculating values for the central PAH filter (f_{p2}) and the PAH-contaminated flanking filter (f_{p3}), yielding: $k = f_{p2}/f_{p3}$. Decomposing the spectrum into PAH and continuum components can be complex and requires careful treatment, however. Below, we outline the strengths and limitations of our various approaches, including the differences between the D21 PAH model spectra and the empirical spectra from PDRs4All.

The D21 models report a PAH emission spectrum as a function of the radiation field, PAH grain size distribution, column density of hydrogen, and PAH charge distribution. Using these models allows us to study how k may change based on the properties of the PAHs, as band ratios of particular PAH features vary depending on the physical conditions of the PAH population. The top panel of Figure 7 shows an example of a D21 model, with a radiation field $\log(U) = 1$ and standard PAH grain size and ionization distributions. To fit the continuum, we mask regions of the spectrum containing PAH emission and fit either a first (for F335M and F770W) or sixth order (for F1130W) polynomial to identify and remove the continuum. We repeat this process across the grids of D21 models, varying the size, ionization, and radiation intensity up to $U = 4$. Figure 8 presents k for each filter trio and shows how it varies depending on the properties of the PAH population. The final k value is the mean of the distribution and the standard deviation is used as the uncertainty to represent the systematic uncertainty in k .

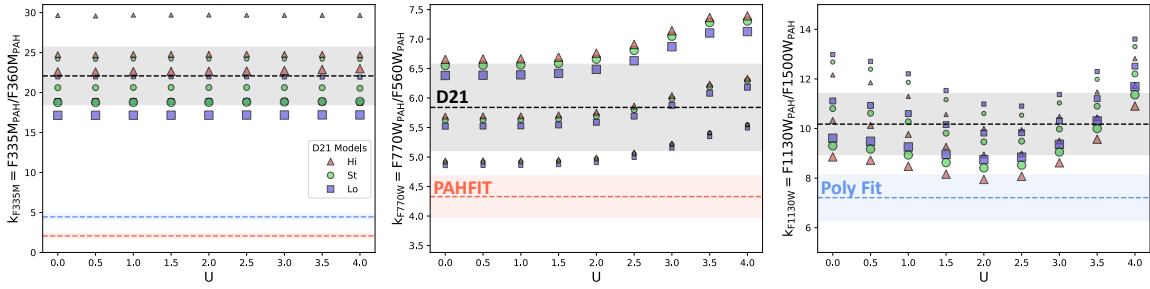


Fig. 8 Estimating the contamination in the flanking PAH filters for continuum subtraction The MIR spectrum is rich in PAH features, making it difficult to identify a true “continuum” bracketing filter required for an accurate continuum subtraction of PAH emission. We estimate the degree of PAH contamination using template spectra from D21 models and the Orion Bar PDRs4All team [102–105]. The contamination constant, k , is equal to the amount of PAH emission in the main PAH filter— F335M (left), F770W (middle), or F1130W (right)— divided by the amount of PAH emission in the contaminated continuum filter— F360M (left), F560W (middle), or F1500W (right). We report the values of k from the D21 grids as a function of ionizing intensity, U . The properties of the PAHs are represented by the points, where the red triangle shows high ionization PAHs, the green circle is standard, and the blue square is low. The size of the points corresponds to the PAH grain size distribution grid. The dashed black line is the average of the D21 models and the standard deviation is given in the gray region. We also show results from the PDRs4All template spectra fits, where the red dashed line uses the PAHFITs from Van De Putte et al. [105] and the blue dashed line uses a simple polynomial to fit and remove the continuum.

The D21 models provide an estimate of how k can change depending on the PAH properties, but not all of the PAH features are accurately captured in the models. Crucially, the models do not include the $3.4 \mu\text{m}$ aliphatic feature or the broader $3.3 \mu\text{m}$ PAH complex. Therefore, we additionally estimate k with empirical JWST spectra of the Orion Bar from the PDRs4All ERS project [102–105], which provide five template spectra from the strip taken along the PDR in Orion from NIRSpec and MIRI-MRS on JWST (see Chown et al. [102] for more details). The empirical spectra from the Orion Bar also provide an independent estimate of k for the two filter trios that focus on the $7.7 \mu\text{m}$ and $11.3 \mu\text{m}$ PAH features. We work with template spectra that have emission lines removed through the line identification presented in Van De Putte et al. [103, 105] and provide two methods of fitting the spectra. The first follows the same approach to fitting the D21 models, where we mask out the regions of the spectrum that contain PAH emission and fit either a first (for F335M and F770W) or sixth order (for F1130W) polynomial to identify and remove the continuum. The second approach uses the code PAHFIT [10] to simultaneously fit

the complex infrared spectrum, including the hot dust continuum, individual PAH features, the stellar continuum, and emission lines. The details of the PDRs4All PAHFITs are presented in Van De Putte et al. [105]. We then apply synthetic photometry on the PAH portion of each spectrum to calculate k for each filter trio for the five template spectra and report the results in Figure 8, where the mean and standard deviation is shown in the spread along the y-axis.

Since the infrared spectrum is quite complex and challenging to fit, we evaluate two approaches for calculating k values for each filter trio, depending on how well each method fits the particular area of the spectrum. The rationale for each choice is described below, and the resulting values are listed in Table 2. We also provide the conversion factor needed to translate PAH fluxes between the two adopted k values. We note that Equation 5 shows that the relationship between k and the PAH flux is non-linear: smaller k values indicate greater contamination in the flanking filter, making the derived PAH flux more sensitive to changes in k when the value is small. By providing two estimates of k , we aim to capture one of the primary sources of systematic uncertainty in the continuum subtraction. Future spectroscopic observations will be required to determine the true PAH flux in each filter.

Table 2 PAH contamination constants for continuum subtraction

Filter Trio	k_1	k_2	Conversion Factor
F300M/F335M/F360M	PDRs4All PAHFIT $k = 2.07 \pm 0.30$	PDRs4All Polyfit $k = 4.45 \pm 0.39$	0.826
F560W/F770W/F1000W	PDRs4All PAHFIT $k = 4.33 \pm 0.35$	Draine2021 $k = 5.84 \pm 0.73$	0.965
F1000W/F1130W/F1500W	PDRs4All Polyfit $k = 7.21 \pm 0.92$	Draine2021 $k = 10.17 \pm 1.24$	0.991

Table Notes: The contamination constants used for each filter trio in this work and the method used to derive them; k_1 is the adopted value used throughout the paper. PAH fluxes derived from k_1 can be converted to k_2 using the provided factor.

F300M/F335M/F360M

The D21 k estimates are not useful for these filters because the models do not contain a $3.4 \mu\text{m}$ feature or broader $3.3 \mu\text{m}$ PAH complex (see Figures 7 and 8). Instead, we use the polynomial fit and PAHFIT of the PDRs4All data to estimate k . With a value of $k = F335M_{\text{PAH}}/F360M_{\text{PAH}} = 2.07 \pm 0.30$, the PAHFIT method estimates more than a factor of two higher level of contamination than the polynomial fit, which report a value of $k = F335M_{\text{PAH}}/F360M_{\text{PAH}} = 4.45 \pm 0.39$ (lower k values implies larger amounts of contamination). This is because the region between $3.3 - 5 \mu\text{m}$ contains a variety of low amplitude, broad, PAH features that create a “PAH continuum” or plateau of PAH emission [6, 138–140]. For the polynomial fit, these features are considered continuum and are removed, but they are treated as PAH features for the PAHFIT method. The PAHFIT approach is also close to the slope of 1.6 reported in Sandstrom et al. [71]. In this work, the PAH contamination in the F360M filter is found by identifying the F335M/F360M ratio in PAH dominated regions through comparing the expected color of PAH emission vs the color of hot dust and stellar continuum. The slope of 1.6 is comparable to the k value calculated through PAHFIT, which is consistent with the explanation of low amplitude PAH features contributing to the F360M PAH filter flux.

We select $k = F335M_{\text{PAH}}/F360M_{\text{PAH}} = 2.07 \pm 0.30$ as the contamination constant to use throughout this work in order to be consistent with the method in Sandstrom et al. [71] and the implementation in Dale et al. [109]. The $3.3 \mu\text{m}$ feature is 21% brighter with this choice of k when compared to PAHFIT $k = F335M_{\text{PAH}}/F360M_{\text{PAH}} = 4.45 \pm 0.39$, leading to a systematic uncertainty on the PAH flux assumed through this work.

F560W/F770W/F1000W

For this filter trio, we use the k based on the D21 models and the PAHFIT of the PDRs4All template spectra, which exhibit a difference of 35% depending on the properties of the PAHs. The variation stems from the PDRs4All spectra having systematically brighter 5.3 , 5.6 , and $6.3 \mu\text{m}$ features, while the $7.7 \mu\text{m}$ complex is fainter compared to the D21 models. It is likely that the PAH population in the Orion Bar differs from the population assumed in D21, which was tuned to observations from the extragalactic

sample SINGS [10]. However, the contamination level in F560W is not as high as it is in F360M, so the precise choice of k does not have as large of an impact on the final PAH flux. The PDRs4All PAHFIT data yields $k = F770W_{\text{PAH}}/F560W_{\text{PAH}} = 4.33 \pm 0.35$ while the D21 yields $k = F770W_{\text{PAH}}/F560W_{\text{PAH}} = 5.84 \pm 0.73$. Propagating these values through Equation 5 changes the resulting $7.7 \mu\text{m}$ flux by only $\sim 4\%$, indicating that this systematic uncertainty does not significantly affect our results. We adopt the PDRs4All PAHFIT value, as the $7.7 \mu\text{m}$ feature in Sextans A is under-luminous (see Figure 6 and more consistent with the spectra in the PDRs4All sample.

We compare our approach to Donnelly et al. [135], an independent, empirically-derived continuum subtraction method focused on MIRI filters benchmarked by MIRI/MRS spectra of luminous infrared galaxies. The two methods agree well, with differences of only 5.5% when using the F560W/F770W/F1000W filter trio to derive the total PAH flux in the F770W filter.

F1000W/F1130W/F1500W

Here, we report k values from D21 and the polynomial fit of the PDRs4All data. The PAHFIT for this trio is not used because the modified blackbody in PAHFIT does not adequately fit the Orion Bar in the $15 - 20 \mu\text{m}$ range [105], leading to over-subtraction of PAH features. The sixth order polynomial fits this region nicely, however, so the simple polynomial fit is adopted instead. The difference between $k = F1130W_{\text{PAH}}/F1500W_{\text{PAH}} = 10.17 \pm 1.24$ for the D21 models and $k = F1130W_{\text{PAH}}/F1500W_{\text{PAH}} = 7.21 \pm 0.92$ is due to the D21 models predicting slightly brighter and broader $11.3 \mu\text{m}$ features than is seen in the PDRs4All data. This difference in k is negligible in the flux calculation of $11.3 \mu\text{m}$ PAH flux, however, as it introduces a $< 1\%$ change. We adopt the PDRs4All polynomial fit for this work, but note that the F1000W/F1130W/F1500W is the most robust to this choice of k .

Our continuum subtraction method for F1130W also agrees very well with the approach in Donnelly et al. [135], deriving a difference of only 5.1% between F1130W fluxes from the two methods when using the F1000W/F1130W/F1500W trio.

Limitations of the continuum subtraction method

While our continuum subtraction method provides a robust estimate of PAH fluxes that is consistent with other approaches [e.g. 59, 71, 102, 133, 135], several limitations should be noted. First, the template spectra used to estimate the continuum may not accurately represent the conditions in Sextans A; for example, Figure 6 shows that the $7.7 \mu\text{m}$ feature is under-luminous compared to both the D21 model grids and the PDRs4All data. Second, some filters assumed to measure just the continuum are not entirely free of PAH emission or other features: the F1000W filter, for instance, captures low-level PAH emission in its wings and may also include a weak silicate feature [e.g., 10]. Additionally, the continuum may not be well approximated as linear, particularly in the F1000W/F1130W/F1500W filter trio where stochastically heated hot dust can dominate and manifests as a powerlaw rather than linear continuum. Furthermore, the method presented here reports *all* the PAH flux within a given filter and does not explicitly separate contributions from adjacent PAH features that are partially captured in the filter bandpass. For example, the F770W filter also includes flux from the $8.3 \mu\text{m}$ feature, and the $3.3 \mu\text{m}$ filter may contain a contribution from the $3.4 \mu\text{m}$ aliphatic feature, if present. Lastly, ionized gas emission lines will contaminate some filters, although the contribution is generally low $< 10\%$ except in extreme cases near in very bright HII regions [e.g. 58, 141, 142]. While our photometric continuum subtraction provides robust estimates of PAH fluxes, it cannot fully account for all systematic uncertainties arising from the effects discussed above. Upcoming Cycle 4 JWST NIRSpec and MIRI MRS spectroscopic observations (GO 7396, PI: E. Tarantino) will help address these systematics, enabling a more precise determination of the PAH band strengths.

3.1.5 Estimate of Uncertainties

While the JWST pipeline reports a drizzled variance array, the noise properties of the JWST images depend on the spatial resolution and become covariant after PSF matching and resampling to a common grid (see Section 3.1.3) since the noise is correlated at a pixel level. Therefore, we calculate the noise and resulting uncertainties in the PSF matched images themselves, similar to the approach in Chown et al. [54] and explored in Williams et al. [143]. We identify a region in the image that is relatively signal free, besides a few stars (centered at RA=10h11m08.2s; DEC= -4d42m41.6s). We sigma-clip with 5 iterations

to remove these stars and calculate the root mean squared (RMS) noise within the region, which serves as the 1σ level uncertainty for all PSF matched images.

We propagate the uncertainties of each PSF-matched filter when calculating the continuum subtracted PAH images, described in Section 3.1.4. We also consider the uncertainty in the estimated value of k by including the standard deviation of the variation in k values as an additional uncertainty that is propagated through the continuum subtraction equation.

3.2 Ancillary Data

We present H α observations of Sextans A from the LVL survey [72, 99] as well as *Swift* UVOT observations [144] to provide a high resolution ($\sim 1.1''$ for H α ; $\sim 2.5''$ for UV) comparison to the ionized gas and the UV radiation field in Sextans A. We converted the LVL H α map from counts into $\text{erg s}^{-1} \text{cm}^{-2}$ using the documentation outlined for the DR5 LVL data release⁴. We then removed the contribution of the [NII] doublet from the narrowband imaging by assuming a ratio of [NII]/H α = 0.04 from Kennicutt et al. [72]. The H α image is displayed in Figure 3. The *Swift* UVOT data were reduced with the method outlined in Hagen et al. [144] and we use this UV data as a secondary measure of the radiation field near the PAH clumps.

3.3 Clump identification

The spatial distribution of PAH emission in Sextans A closely resembles the hierarchical structure captured by dendrograms, where a larger “trunk” encompasses several “leaf” structures that lack further substructure (see Figures 3 and 4). Dendrograms are commonly employed to characterize the fragmentation of molecular clouds, dust, and other ISM tracers [e.g., 145–147]. Given this, it is reasonable to represent the PAH morphology in Sextans A using a dendrogram-based framework. The main purpose of using dendrograms is to have a uniform procedure in defining the clump boundaries and properties. We utilize the *astrodendro* package to define the boundaries of these clumps and calculate their properties, such as the shape, integrated flux, and deconvolved size of the clumps.

First, we identify an initial catalog by requiring each clump of emission to have a 3σ detection or higher in each of the $3.3 \mu\text{m}$, $7.7 \mu\text{m}$, and $11.3 \mu\text{m}$ continuum subtracted PAH images. This insures that the PAH clump detection is robust as it is seen in all three features and not a spurious high redshift galaxy. We adopt the $7.7 \mu\text{m}$ continuum subtracted PAH data to define the clump structure, as clump sizes differ slightly between bands, and $7.7 \mu\text{m}$ provides a consistent standard being central between 3.3 and $11.3 \mu\text{m}$. The minimum value of the dendrogram is set to be the 1σ noise level of the $7.7 \mu\text{m}$ continuum subtracted PAH data, ensuring the noise is pruned from the final structure. The minimum significance for structures (`min_delta`) is set to the 3σ level, requiring each structure and sub-structure to have at least three times the noise level to be defined as a clump. Each clump is required to be at least 4 pixels in size, about the size of the FWHM of all the PSF matched images. We cross match the dendrogram structure list with the initial clump catalog and include only the clumps that pass the initial cut of a $> 3\sigma$ detection in all three continuum subtracted PAH data.

The resulting catalog of clumps is presented in Table 1 and the clumps are plotted on the JWST images in Figure 3. All size measurements are deconvolved with the size of the PSF FWHM ($0.488''$). We use the $7.7 \mu\text{m}$ dendrogram clump boundaries and calculate the integrated PAH flux of the other two features from the $3.3 \mu\text{m}$ and $11.3 \mu\text{m}$ continuum subtracted PAH data, ensuring equivalent area and boundaries for each clump definition. The dendrogram analysis mostly identifies “leaf” structures, which do not have additional substructure, with the exception of clumps 15 and 16 that are the larger “trunks” encompassing the two of the smaller leaves. Interestingly, most of the PAH structures identified in the dendrogram are individual leaves, which contrasts with observations of higher metallicity galaxies, where PAH emission is typically more extended, highly structured, and closely traces the bulk of the ISM [e.g., 18, 36, 74, 148]. In Sextans A, however, the PAH distribution is compact and point-like, with only two resolved PAH structures located within the JWST observations of the galaxy.

⁴https://irsa.ipac.caltech.edu/data/SPITZER/LVL/doc/LVL_DR5_v5.pdf

3.4 Modeling the infrared spectrum

The infrared spectrum from $1 - 15 \mu\text{m}$ is complex, containing contributions from stellar light, PAH emission, and hot dust. The multiband JWST NIRCam and MIRI photometry of Sextans A comprises eleven filters that sample the spectrum across the $1 - 15 \mu\text{m}$ baseline. We model the flux in clump 1 (see Table 1) using a combination of stellar and dust models⁵. First, we select the short wavelength NIRCam filters (F115W, F150W, and F200W) and identify the best fitting stellar models using grids from high-resolution synthetic spectra based on the stellar atmosphere code PHOENIX [70]. We apply synthetic photometry through the `synphot` package, which implements Equation 5 in [149] to calculate the photon weighted average flux density through a given photometric filter. For clump 1, the best fitting model with a $\chi^2 = 3$ has a metallicity of $[M/H] = -1.15$, a temperature of $T = 6600 \text{ K}$, surface gravity of $\log(g) = 0.0 \text{ cm s}^{-1}$, and a normalization constant of $\log(C) = 35.1$. We set this PHOENIX stellar model as the stellar portion of the SED, which dominates the $1 - 5 \mu\text{m}$ portion of the spectrum.

For the PAH emission and hot dust, we use the physically motivated D21 models, which contain PAH particles of varying sizes and a population of larger “astrodust” grains from [150] for the hot dust continuum. These models predict a MIR spectrum from a variety of input illuminating radiation fields and model the influence of size and ionization distribution of the PAHs on their emission features. We use the low metallicity $Z = 0.0004 \approx 0.02Z_{\odot}$, 10 Myr burst from Bruzual and Charlot [100] as the input radiation spectral shape to match the low metallicity conditions in Sextans A. We then create a grid of D21 models by varying the radiation field intensity (U), PAH-to-dust mass fraction q_{PAH} , column density of hydrogen (N_{H}), the ionization state of the PAHs, and the size of the PAHs. The PHOENIX stellar model derived above is added to each D21 spectra and we apply synthetic photometry for the rest of the JWST filters (F300M, F335M, F360M, F560W, F770W, F1000W, F1130W, and F1500W). We calculate the best fit through χ^2 , which tend to be large, as the uncertainties on the filter fluxes are quite low. We identify models that have $\chi^2 < 10000$ to be the models that provide the best fit and plot the MIR spectra in Figure 2 as the gray lines, where the transparency corresponds to the χ^2 . The average of all the spectra is presented as the dark black line.

There isn’t a single D21 model that well produces the observed SED in Sextans A, as one that matches one filter may not match another, i.e., fitting F770W well leads to an under prediction in F1000W and F1500W. The mismatch between the JWST photometry and D21 models could be due to variety of effects, including: emission from bright emission lines contaminating a given filter (e.g., [SIV] in F1000W), absorption from silicates at $10 \mu\text{m}$, and/or that PAHs fluxes or profiles at these very low 7% Solar metallicities vary significantly from their high metallicity counterparts. The D21 models were tested with spectra from the Spitzer Infrared Nearby Galaxy Survey (SINGS) [10, 88] and AKARI [106], which are biased towards the centers of typical, high metallicity star-forming galaxies. Future Cycle 4 JWST spectroscopic observations of Sextans A (GO 7396, PI: E. Tarantino) will help disentangle the origin of these differences.

The D21 fits to the SED favor low values of q_{PAH} , ranging from $q_{\text{PAH}} = 0.2 - 0.9$, consistent with observations of metal-poor dwarf galaxies [28, 34–36]. The intensity of the radiation field varies from $\log U = 0 - 3.5$, without much dependence for a particular value, but models with $\log U > 3.5$ do not fit the SED well. These reported properties should be interpreted with caution, as the D21 models do not fully reproduce the JWST observations. Future work that incorporates spectroscopic data and applies a statistically rigorous treatment of the free parameters in the D21 models will enable a more accurate assessment of the PAH properties in Sextans A.

3.5 Radial profile of a PAH clump

To examine how the spatial distribution of the PAH emission compares to that of the hot dust, we calculate radial profiles of the PAH clumps defined by the dendrogram structures in Section 3.3. We use the F1500W filter as a measure of the hot dust continuum as observations with the F2100W filter do not exist for Sextans A. In Figure 9, we present the radial profile of clump 15, defined as the azimuthally-averaged flux in circular annuli apertures as a function of radius from the clump center (see Table 1). Clump 15 (see Figure 3) is the largest and brightest clump that encompasses two smaller PAH structures and is the prominent structure highlighted in Figure 4. We plot the radial profile of the $11.3 \mu\text{m}$ PAH

⁵We note that our goal is to provide an approximate fit to the photometric data for Figure 2, a more in depth evaluation of the plausible parameter space for the models will be explored in future work.

emission, the continuum at $11.3\ \mu\text{m}$, and the F1500W hot dust continuum emission and normalize each profile so the sum is equal to one. The resulting radial profiles show that emission from PAHs peaks at the center, decreases slightly, then increases again due to the second PAH structure internal in the larger clump of emission. The PAH emission then falls off to the 1σ noise level at larger radii. In contrast, the F1500W emission increases in between the peaks of the two PAH clumps encompassed in this structure (likely due to the extended spatial distribution of the dust), then the emission overall decreases but to a level 2.5σ above the noise floor in F1500W, signifying that there is extended emission in the hot dust continuum not present in the PAH emission. A similar profile is seen in the continuum at $11.3\ \mu\text{m}$, but does not peak as high in between the two smaller clump structures.

The extended nature of both the F1500W filter and continuum at $11.3\ \mu\text{m}$ signifies that PAH emission is more compact than the dust and supports the argument in Section 2 that the resolved $\Sigma\text{PAH}/\text{TIR}$ ratio is likely affected by beam smearing from the large $\sim 30''$ spatial resolution of the FIR data. However, it is difficult to quantify the degree to which the PAH emission is more compact than the overall dust distribution. Future work involving high resolution dust extinction mapping [e.g. 151–153] and observations of the F2100W filter from GO 7396 (PI: E. Tarantino) will help illuminate the spatial scale of the PAH emission relative to other ISM tracers.

3.6 Calculating the $3.3\ \mu\text{m}/11.3\ \mu\text{m}$ and $3.3\ \mu\text{m}/7.7\ \mu\text{m}$ Band Ratios

We investigate the size and ionization state of the PAHs in Sextans A by calculating the continuum subtracted $3.3\ \mu\text{m}/11.3\ \mu\text{m}$ and $3.3\ \mu\text{m}/7.7\ \mu\text{m}$ band ratios for the clump catalog in Table 1. We compare measured band ratios with the models from D21 that use the low metallicity $Z = 0.0004 \approx 0.02Z_{\odot}$, 10 Myr burst from Bruzual and Charlot [100] as the input spectrum. The PAH size distribution in D21 is modeled as a sum of two log normal size distributions, where the “small”, “standard”, and “large” models correspond to a peak size in the distribution at 3\AA , 4\AA , and 5\AA , respectively (see Figure 9 and Equation 15 in D21). The charge of the PAHs are separated into the “standard” model, which uses the ionization fraction given in Draine and Li [101], as well as “low” and “high” models which have a factor of two shift lower and higher in the f_{ion} respectively. We average the D21 model grids from $\log U = 0 - 3.5$, since the radiation field does not impact the PAH band ratios until high radiation fields at $\log U \gtrsim 4$ [69].

We apply synthetic photometry to the D21 models for all the filters centered on PAH emission (F335M, F770W, and F1130W), as well as the bracketing continuum filters, and calculate the continuum subtracted PAH emission for the $3.3\ \mu\text{m}$, $7.7\ \mu\text{m}$, and $11.3\ \mu\text{m}$ features. The same continuum subtraction method is used for both the D21 models and the JWST data; however, for the models, we adopt the contamination constant, k , derived specifically from the D21 spectra. This choice has a negligible effect on the continuum subtraction at $7.7\ \mu\text{m}$ and $11.3\ \mu\text{m}$. However, it significantly affects the $3.3\ \mu\text{m}$ measurement: because the D21 models do not include the nearby $3.4\ \mu\text{m}$ feature, applying a k value derived from PDRs4All data (which does include $3.4\ \mu\text{m}$ emission) would result in a negative continuum estimate at $3.3\ \mu\text{m}$ in the D21 models. The results are presented in Figure 6.

Acknowledgments. This work is based on observations made with the NASA/ESA/CSA James Webb Space Telescope. The data were obtained from the Mikulski Archive for Space Telescopes at the Space Telescope Science Institute, which is operated by the Association of Universities for Research in Astronomy, Inc., under NASA contract NAS5-03127 for JWST. These observations are associated with program GO-2391. We acknowledge Interstellar Institute programmes and Paris-Saclay Universitys Institut Pascal for hosting discussions that nourished the development of the ideas behind this work. We acknowledge the NRAO and Research Corporation for their support of the PAH Workshop in Charlottesville, Virginia. This research was carried out in part at the Jet Propulsion Laboratory, California Institute of Technology, under a contract with the National Aeronautics and Space Administration (80NM0018D0004). O.G.T. acknowledges support from a Carnegie-Princeton Fellowship through Princeton University and the Carnegie Observatories.

References

- [1] Kwok, S., Zhang, Y.: Mixed aromatic-aliphatic organic nanoparticles as carriers of unidentified infrared emission features. *Nature* **479**(7371), 80–83 (2011) <https://doi.org/10.1038/nature10542>

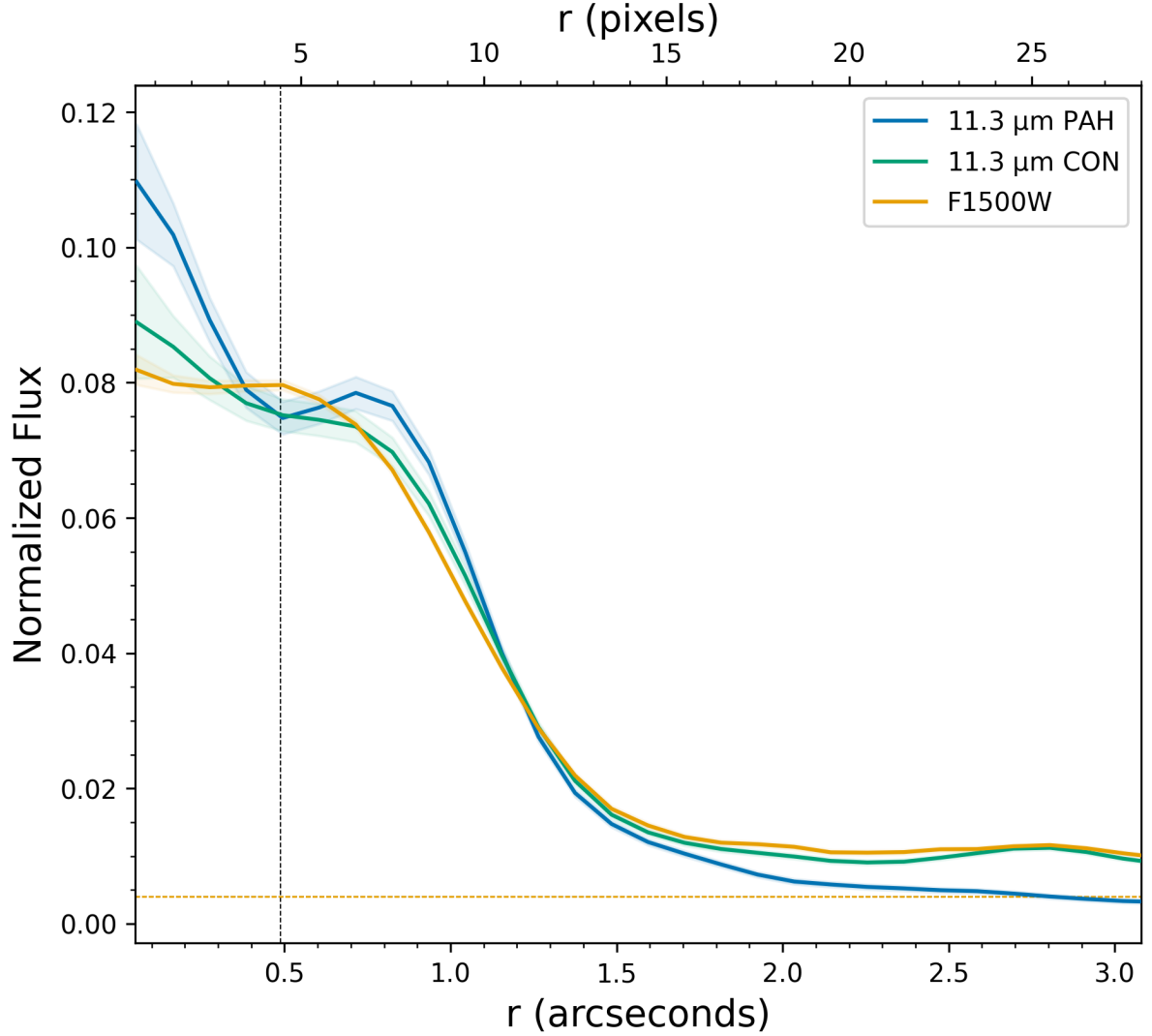


Fig. 9 Radial profile of the most extended and brightest PAH emission structure, clump 15 We present the $11.3\ \mu\text{m}$ PAH flux in blue, the continuum at $11.3\ \mu\text{m}$ in green, and the F1500W filter as a tracer of hot dust in orange. Each profile is the azimuthally averaged flux in a circular annular aperture, where the center is the clump defined by the dendrogram structure analysis (see Section 3.3). The profiles are normalized so the sum is equal to one. The FWHM of the $0.488''$ PSF is given by the vertical dashed black line and the 1σ level uncertainty for each profile are the horizontal dashed lines (they all overlap in this scaling). The PAH emission profile peaks towards the center of the PAH clump, falls off before reaching another peak when the azimuthal averages passes through a clump local maximum, and then declines to the 1σ noise floor. The continuum and F1500W profiles instead continue to a level 2.5σ above, signifying that they trace more extended emission than the PAH profile.

- [2] Li, A., Draine, B.T.: The Carriers of the Interstellar Unidentified Infrared Emission Features: Aromatic or Aliphatic? *Astrophys. J.* **760**, 35 (2012) <https://doi.org/10.1088/2041-8205/760/2/L35>
- [3] Yang, X.J., Glaser, R., Li, A., Zhong, J.X.: The Carriers of the Interstellar Unidentified Infrared Emission Features: Constraints from the Interstellar C-H Stretching Features at 3.2-3.5 Mm . *Astrophys. J.* **776**, 110 (2013) <https://doi.org/10.1088/0004-637X/776/2/110>
- [4] Knacke, R.F.: Carbonaceous compounds in interstellar dust. *Nature* **269**(5624), 132–134 (1977) <https://doi.org/10.1038/269132a0>
- [5] Allamandola, L.J., Tielens, A.G.G.M., Barker, J.R.: Polycyclic aromatic hydrocarbons and the

- unidentified infrared emission bands: Auto exhaust along the milky way. *Astrophys. J. Lett.* **290**, 25–28 (1985) <https://doi.org/10.1086/184435>
- [6] Allamandola, L.J., Tielens, A.G.G.M., Barker, J.R.: Interstellar Polycyclic Aromatic Hydrocarbons: The Infrared Emission Bands, the Excitation/Emission Mechanism, and the Astrophysical Implications. *Astrophys. J. Suppl. Ser.* **71**, 733 (1989) <https://doi.org/10.1086/191396>
- [7] Tielens, A.G.G.M.: Interstellar polycyclic aromatic hydrocarbon molecules. *Annu. Rev. Astron. Astrophys.* **46**, 289–337 (2008) <https://doi.org/10.1146/annurev.astro.46.060407.145211>
- [8] Li, A.: Spitzer’s perspective of polycyclic aromatic hydrocarbons in galaxies. *Nat. Astron.* **4**, 339–351 (2020) <https://doi.org/10.1038/s41550-020-1051-1>
- [9] Helou, G., Lu, N.Y., Werner, M.W., Malhotra, S., Silbermann, N.: The Mid-Infrared Spectra of Normal Galaxies. *Astrophys. J. Lett.* **532**(1), 21–24 (2000) <https://doi.org/10.1086/312549>
- [10] Smith, J.D.T., Draine, B.T., Dale, D.A., Moustakas, J., Kennicutt, Jr. R. C., Helou, G., Armus, L., Roussel, H., Sheth, K., Bendo, G.J., Buckalew, B.A., Calzetti, D., Engelbracht, C.W., Gordon, K.D., Hollenbach, D.J., Li, A., Malhotra, S., Murphy, E.J., Walter, F.: The Mid-Infrared Spectrum of Star-forming Galaxies: Global Properties of Polycyclic Aromatic Hydrocarbon Emission. *Astrophys. J.* **656**(2), 770–791 (2007) <https://doi.org/10.1086/510549>
- [11] Peeters, E., Spoon, H.W.W., Tielens, A.G.G.M.: Polycyclic Aromatic Hydrocarbons as a Tracer of Star Formation? *Astrophys. J.* **613**(2), 986–1003 (2004) <https://doi.org/10.1086/423237>
- [12] Shipley, H.V., Papovich, C., Rieke, G.H., Brown, M.J.I., Moustakas, J.: A New Star Formation Rate Calibration from Polycyclic Aromatic Hydrocarbon Emission Features and Application to High-redshift Galaxies. *Astrophys. J.* **818**(1), 60 (2016) <https://doi.org/10.3847/0004-637X/818/1/60>
- [13] Gregg, B., Calzetti, D., Adamo, A., Bajaj, V., Ryon, J.E., Linden, S.T., Correnti, M., Cignoni, M., Messa, M., Sabbi, E., Gallagher, J.S., Grasha, K., Pedrini, A., Gutermuth, R.A., Melinder, J., Kotulla, R., Pérez, G., Krumholz, M.R., Bik, A., Östlin, G., Johnson, K.E., Bortolini, G., Smith, L.J., Tosi, M., Maji, S., Faustino Vieira, H.: Feedback in Emerging Extragalactic Star Clusters, FEAST: The Relation between 3.3 Mm Polycyclic Aromatic Hydrocarbon Emission and Star Formation Rate Traced by Ionized Gas in NGC 628. *ApJ* **971**(1), 115 (2024) <https://doi.org/10.3847/1538-4357/ad54b4>
- [14] Ronayne, K., Papovich, C., Yang, G., Shen, L., Dickinson, M., Kennicutt, R., Alavi, A., Arrabal Haro, P., Bagley, M.B., Burgarella, D., Le Bail, A., Bell, E.F., Cleri, N.J., Cole, J., Costantin, L., de la Vega, A., Daddi, E., Elbaz, D., Finkelstein, S.L., Grogin, N.A., Holwerda, B.W., Kartaltepe, J.S., Kirkpatrick, A., Koekemoer, A.M., Lucas, R.A., Magnelli, B., Mobasher, B., Pérez-González, P.G., Prichard, L., Rafelski, M., Rodighiero, G., Sunnquist, B., Teplitz, H.I., Wang, X., Windhorst, R.A., Yung, L.Y.A.: CEERS: 7.7 Mm PAH Star Formation Rate Calibration with JWST MIRI. *Astrophys. J.* **970**, 61 (2024) <https://doi.org/10.3847/1538-4357/ad5006>
- [15] Cortzen, I., Garrett, J., Magdis, G., Rigopoulou, D., Valentino, F., Pereira-Santaella, M., Combes, F., Alonso-Herrero, A., Toft, S., Daddi, E., Elbaz, D., Gómez-Guijarro, C., Stockmann, M., Huang, J., Kramer, C.: PAHs as tracers of the molecular gas in star-forming galaxies. *Mon. Not. R. Astron. Soc.* **482**(2), 1618–1633 (2019) <https://doi.org/10.1093/mnras/sty2777>
- [16] Leroy, A.K., Bolatto, A.D., Sandstrom, K., Rosolowsky, E., Barnes, Ashley.T., Bigiel, F., Boquien, M., den Brok, J.S., Cao, Y., Chastenet, J., Chevance, M., Chiang, I.-D., Chown, R., Colombo, D., Ellison, S.L., Emsellem, E., Grasha, K., Henshaw, J.D., Hughes, A., Klessen, R.S., Koch, E.W., Kim, J., Kreckel, K., Kruijssen, J.M.D., Larson, K.L., Lee, J.C., Levy, R.C., Lin, L., Liu, D., Meidt, S.E., Pety, J., Querejeta, M., Rubio, M., Saito, T., Salim, S., Schinnerer, E., Sormani, M.C., Sun, J., Thilker, D.A., Usero, A., Vogel, S.N., Watkins, E.J., Whitcomb, C.M., Williams, T.G., Wilson,

- C.D.: PHANGS-JWST First Results: A Global and Moderately Resolved View of Mid-infrared and CO Line Emission from Galaxies at the Start of the JWST Era. *Astrophys. J. Lett.* **944**(2), 10 (2023) <https://doi.org/10.3847/2041-8213/acab01>
- [17] Shivaee, I., Boogaard, L.A.: The tight correlation between PAH and CO emission from $z \sim 0$ to 4. *Astron. Astrophys.* **691**, 2 (2024) <https://doi.org/10.1051/0004-6361/202451826>
 - [18] Chown, R., Leroy, A.K., Sandstrom, K., Chasteney, J., Sutter, J., Koch, E.W., Koziol, H.B., Neumann, L., Sun, J., Williams, T.G., Baron, D., Anand, G.S., Barnes, Ashley.T., Bazzi, Z., Belfiore, F., Bigiel, F., Bolatto, A., Boquien, M., Cao, Y., Chevance, M., Colombo, D., Dale, D.A., den Brok, J., Egorov, O.V., Eibensteiner, C., Emsellem, E., Hassani, H., Henshaw, J.D., He, H., Kim, J., Klessen, R.S., Kreckel, K., Larson, K.L., Lee, J.C., Meidt, S.E., Murphy, E.J., Oakes, E.K., Ostriker, E.C., Pan, H.-A., Pathak, D., Rosolowsky, E., Sarbadhicary, S.K., Schinnerer, E., Teng, Y.-H., Thilker, D.A., Weinbeck, T.D., Watkins, E.J.: Polycyclic Aromatic Hydrocarbon and CO(2–1) Emission at 50–150 pc Scales in 70 Nearby Galaxies. *Astrophys. J.* **983**, 64 (2025) <https://doi.org/10.3847/1538-4357/adbd40>
 - [19] Bakes, E.L.O., Tielens, A.G.G.M.: The Photoelectric Heating Mechanism for Very Small Graphitic Grains and Polycyclic Aromatic Hydrocarbons. *Astrophys. J.* **427**, 822 (1994) <https://doi.org/10.1086/174188>
 - [20] Wolfire, M.G., Hollenbach, D., McKee, C.F., Tielens, A.G.G.M., Bakes, E.L.O.: The Neutral Atomic Phases of the Interstellar Medium. *Astrophys. J.* **443**, 152 (1995) <https://doi.org/10.1086/175510>
 - [21] Weingartner, J.C., Draine, B.T.: Dust Grain-Size Distributions and Extinction in the Milky Way, Large Magellanic Cloud, and Small Magellanic Cloud. *Astrophys. J.* **548**(1), 296–309 (2001) <https://doi.org/10.1086/318651>
 - [22] Reach, W.T., Boulanger, F., Contursi, A., Lequeux, J.: Detection of mid-infrared aromatic hydrocarbon emission features from the Small Magellanic Cloud. *Astron. Astrophys.* **361**, 895–900 (2000) <https://doi.org/10.48550/arXiv.astro-ph/0007382>
 - [23] Houck, J.R., Charmandaris, V., Brandl, B.R., Weedman, D., Herter, T., Armus, L., Soifer, B.T., Bernard-Salas, J., Spoon, H.W.W., Devost, D., Uchida, K.I.: The Extraordinary Mid-infrared Spectrum of the Blue Compact Dwarf Galaxy SBS 0335-052. *Astrophys. J. Suppl. Ser.* **154**(1), 211–214 (2004) <https://doi.org/10.1086/423137>
 - [24] Engelbracht, C.W., Gordon, K.D., Rieke, G.H., Werner, M.W., Dale, D.A., Latter, W.B.: Metallicity Effects on Mid-Infrared Colors and the 8 μ m PAH Emission in Galaxies. *Astrophys. J. Lett.* **628**(1), 29–32 (2005) <https://doi.org/10.1086/432613>
 - [25] Engelbracht, C.W., Rieke, G.H., Gordon, K.D., Smith, J.-D.T., Werner, M.W., Moustakas, J., Willmer, C.N.A., Vanzì, L.: Metallicity Effects on Dust Properties in Starbursting Galaxies. *Astrophys. J.* **678**(2), 804–827 (2008) <https://doi.org/10.1086/529513>
 - [26] Madden, S.C., Galliano, F., Jones, A.P., Sauvage, M.: ISM properties in low-metallicity environments. *Astron. Astrophys.* **446**(3), 877–896 (2006) <https://doi.org/10.1051/0004-6361:20053890>
 - [27] Jackson, D.C., Cannon, J.M., Skillman, E.D., Lee, H., Gehrz, R.D., Woodward, C.E., Polomski, E.: Hot Dust and Polycyclic Aromatic Hydrocarbon Emission at Low Metallicity: A Spitzer Survey of Local Group and Other Nearby Dwarf Galaxies. *Astrophys. J.* **646**(1), 192–204 (2006) <https://doi.org/10.1086/504707>
 - [28] Wu, Y., Charmandaris, V., Hao, L., Brandl, B.R., Bernard-Salas, J., Spoon, H.W.W., Houck, J.R.: Mid-Infrared Properties of Low-Metallicity Blue Compact Dwarf Galaxies from the Spitzer Infrared Spectrograph. *Astrophys. J.* **639**(1), 157–172 (2006) <https://doi.org/10.1086/499226>

- [29] Draine, B.T., Dale, D.A., Bendo, G., Gordon, K.D., Smith, J.D.T., Armus, L., Engelbracht, C.W., Helou, G., Kennicutt, Jr. R. C., Li, A., Roussel, H., Walter, F., Calzetti, D., Moustakas, J., Murphy, E.J., Rieke, G.H., Bot, C., Hollenbach, D.J., Sheth, K., Teplitz, H.I.: Dust Masses, PAH Abundances, and Starlight Intensities in the SINGS Galaxy Sample. *Astrophys. J.* **663**(2), 866–894 (2007) <https://doi.org/10.1086/518306>
- [30] Galliano, F., Madden, S.C., Jones, A.P., Wilson, C.D., Bernard, J.-P., Le Peintre, F.: ISM properties in low-metallicity environments. II. The dust spectral energy distribution of NGC 1569. *Astron. Astrophys.* **407**, 159–176 (2003) <https://doi.org/10.1051/0004-6361:20030814>
- [31] Galliano, F., Madden, S.C., Tielens, A.G.G.M., Peeters, E., Jones, A.P.: Variations of the Mid-IR Aromatic Features inside and among Galaxies. *Astrophys. J.* **679**(1), 310–345 (2008) <https://doi.org/10.1086/587051>
- [32] Gordon, K.D., Engelbracht, C.W., Rieke, G.H., Misselt, K.A., Smith, J.-D.T., Kennicutt, R.C. Jr.: The Behavior of the Aromatic Features in M101 HII Regions: Evidence for Dust Processing. *ApJ* **682**(1), 336–354 (2008) <https://doi.org/10.1086/589567>
- [33] Marble, A.R., Engelbracht, C.W., van Zee, L., Dale, D.A., Smith, J.D.T., Gordon, K.D., Wu, Y., Lee, J.C., Kennicutt, R.C., Skillman, E.D., Johnson, L.C., Block, M., Calzetti, D., Cohen, S.A., Lee, H., Schuster, M.D.: An Aromatic Inventory of the Local Volume. *Astrophys. J.* **715**(1), 506–540 (2010) <https://doi.org/10.1088/0004-637X/715/1/506>
- [34] Hunt, L.K., Thuan, T.X., Izotov, Y.I., Sauvage, M.: The Spitzer View of Low-Metallicity Star Formation. III. Fine-Structure Lines, Aromatic Features, and Molecules. *Astrophys. J.* **712**(1), 164–187 (2010) <https://doi.org/10.1088/0004-637X/712/1/164>
- [35] Sandstrom, K.M., Bolatto, A.D., Draine, B.T., Bot, C., Stanimirović, S.: The Spitzer Survey of the Small Magellanic Cloud (S³MC): Insights into the Life Cycle of Polycyclic Aromatic Hydrocarbons. *Astrophys. J.* **715**(2), 701–723 (2010) <https://doi.org/10.1088/0004-637X/715/2/701>
- [36] Chastenet, J., Sandstrom, K., Chiang, I.-D., Leroy, A.K., Utomo, D., Bot, C., Gordon, K.D., Draine, B.T., Fukui, Y., Onishi, T., Tsuge, K.: The Polycyclic Aromatic Hydrocarbon Mass Fraction on a 10 pc Scale in the Magellanic Clouds. *Astrophys. J.* **876**(1), 62 (2019) <https://doi.org/10.3847/1538-4357/ab16cf>
- [37] Aniano, G., Draine, B.T., Hunt, L.K., Sandstrom, K., Calzetti, D., Kennicutt, R.C., Dale, D.A., Galametz, M., Gordon, K.D., Leroy, A.K., Smith, J.-D.T., Roussel, H., Sauvage, M., Walter, F., Armus, L., Bolatto, A.D., Boquien, M., Crocker, A., De Looze, I., Donovan Meyer, J., Helou, G., Hinz, J., Johnson, B.D., Koda, J., Miller, A., Montiel, E., Murphy, E.J., Relaño, M., Rix, H.-W., Schinnerer, E., Skibba, R., Wolfire, M.G., Engelbracht, C.W.: Modeling Dust and Starlight in Galaxies Observed by Spitzer and Herschel: The KINGFISH Sample. *Astrophys. J.* **889**(2), 150 (2020) <https://doi.org/10.3847/1538-4357/ab5fdb>
- [38] Whitcomb, C.M., Smith, J.-D.T., Sandstrom, K., Starkey, C.A., Donnelly, G.P., Draine, B.T., Skillman, E.D., Dale, D.A., Armus, L., Hensley, B.S., Lai, T.S.-Y., Kennicutt, R.C.: The Metallicity Dependence of PAH Emission in Galaxies. I. Insights from Deep Radial Spitzer Spectroscopy. *Astrophys. J.* **974**, 20 (2024) <https://doi.org/10.3847/1538-4357/ad66c8>
- [39] Rémy-Ruyer, A., Madden, S.C., Galliano, F., Galametz, M., Takeuchi, T.T., Asano, R.S., Zhukovska, S., Lebouteiller, V., Cormier, D., Jones, A., Bocchio, M., Baes, M., Bendo, G.J., Boquien, M., Boselli, A., DeLooze, I., Doublier-Pritchard, V., Hughes, T., Karczewski, O.L., Spinoglio, L.: Gas-to-dust mass ratios in local galaxies over a 2 dex metallicity range. *Astron. Astrophys.* **563**, 31 (2014) <https://doi.org/10.1051/0004-6361/201322803>
- [40] Micelotta, E.R., Jones, A.P., Tielens, A.G.G.M.: Polycyclic aromatic hydrocarbon processing in a hot gas. *Astron. Astrophys.* **510**, 37 (2010) <https://doi.org/10.1051/0004-6361/200911683>

- [41] Micelotta, E.R., Jones, A.P., Tielens, A.G.G.M.: Polycyclic aromatic hydrocarbon processing in interstellar shocks. *Astron. Astrophys.* **510**, 36 (2010) <https://doi.org/10.1051/0004-6361/200911682>
- [42] Greenberg, J.M., Gillette, J.S., Muñoz Caro, G.M., Mahajan, T.B., Zare, R.N., Li, A., Schutte, W.A., de Groot, M., Mendoza-Gómez, C.: Ultraviolet Photoprocessing of Interstellar Dust Mantles as a Source of Polycyclic Aromatic Hydrocarbons and Other Conjugated Molecules. *Astrophys. J.* **531**, 71–73 (2000) <https://doi.org/10.1086/312526>
- [43] Sandstrom, K.M., Bolatto, A.D., Bot, C., Draine, B.T., Ingalls, J.G., Israel, F.P., Jackson, J.M., Leroy, A.K., Li, A., Rubio, M., Simon, J.D., Smith, J.D.T., Stanimirović, S., Tielens, A.G.G.M., van Loon, J.T.: The Spitzer Spectroscopic Survey of the Small Magellanic Cloud (S4MC): Probing the Physical State of Polycyclic Aromatic Hydrocarbons in a Low-metallicity Environment. *Astrophys. J.* **744**, 20 (2012) <https://doi.org/10.1088/0004-637X/744/1/20>
- [44] Zhukovska, S., Gail, H.-P., Trieloff, M.: Evolution of interstellar dust and stardust in the solar neighbourhood. *Astron. Astrophys.* **479**, 453–480 (2008) <https://doi.org/10.1051/0004-6361:20077789>
- [45] Jones, A.P., Tielens, A.G.G.M., Hollenbach, D.J., McKee, C.F.: The propagation and survival of interstellar grains. In: Bernatowicz, T.J., Zinner, E. (eds.) *Astrophys. Implic. Lab. Study Presolar Mater.* American Institute of Physics Conference Series, vol. 402, pp. 595–613. AIP, ??? (1997). <https://doi.org/10.1063/1.53337>
- [46] Rau, S.-J., Hirashita, H., Murga, M.: Modelling the evolution of PAH abundance in galaxies. *Mon. Not. R. Astron. Soc.* **489**(4), 5218–5224 (2019) <https://doi.org/10.1093/mnras/stz2532>
- [47] Madau, P., Dickinson, M.: Cosmic Star-Formation History. *Annu. Rev. Astron. Astrophys.* **52**, 415–486 (2014) <https://doi.org/10.1146/annurev-astro-081811-125615>
- [48] Witstok, J., Shivaie, I., Smit, R., Maiolino, R., Carniani, S., Curtis-Lake, E., Ferruit, P., Arribas, S., Bunker, A.J., Cameron, A.J., Charlot, S., Chevillard, J., Curti, M., de Graaff, A., D'Eugenio, F., Giardino, G., Looser, T.J., Rawle, T., Rodríguez del Pino, B., Willott, C., Alberts, S., Baker, W.M., Boyett, K., Egami, E., Eisenstein, D.J., Endsley, R., Hainline, K.N., Ji, Z., Johnson, B.D., Kumari, N., Lyu, J., Nelson, E., Perna, M., Rieke, M., Robertson, B.E., Sandles, L., Saxena, A., Scholtz, J., Sun, F., Tacchella, S., Williams, C.C., Willmer, C.N.A.: Carbonaceous dust grains seen in the first billion years of cosmic time. *Nature* **621**, 267–270 (2023) <https://doi.org/10.1038/s41586-023-06413-w>
- [49] Spilker, J.S., Phadke, K.A., Aravena, M., Archipley, M., Bayliss, M.B., Birkin, J.E., Béthermin, M., Burgoyne, J., Cathey, J., Chapman, S.C., Dahle, H., Gonzalez, A.H., Gururajan, G., Hayward, C.C., Hezaveh, Y.D., Hill, R., Hutchison, T.A., Kim, K.J., Kim, S., Law, D., Legin, R., Malkan, M.A., Marrone, D.P., Murphy, E.J., Narayanan, D., Navarre, A., Olivier, G.M., Rich, J.A., Rigby, J.R., Reuter, C., Rhoads, J.E., Sharon, K., Smith, J.D.T., Solimano, M., Sulzenauer, N., Vieira, J.D., Vizgan, D., Weiß, A., Whitaker, K.E.: Spatial variations in aromatic hydrocarbon emission in a dust-rich galaxy. *Nature* **618**(7966), 708–711 (2023) <https://doi.org/10.1038/s41586-023-05998-6>
- [50] Shivaie, I., Alberts, S., Florian, M., Rieke, G., Wuyts, S., Bodansky, S., Bunker, A.J., Cameron, A.J., Curti, M., D'Eugenio, F., Dudzeviciute, U., Kramarenko, I., Ji, Z., Johnson, B.D., Lyu, J., Matthee, J., Morrison, J., Naidu, R., Reddy, N., Robertson, B., Pérez-González, P.G., Sun, Y., Tacchella, S., Whitaker, K., Williams, C.C., Willmer, C.N.A., Witstok, J., Xiao, M., Zhu, Y.: A new census of dust and polycyclic aromatic hydrocarbons at $z=0.7-2$ with JWST MIRI. *A&A* **690**, 89 (2024) <https://doi.org/10.1051/0004-6361/202449579> [arXiv:2402.07989](https://arxiv.org/abs/2402.07989) [astro-ph]
- [51] Hirschauer, A.S., Crouzet, N., Habel, N., Lenkić, L., Nally, C., Jones, O.C., Bortolini, G., Boyer, M.L., Justtanont, K., Meixner, M., Östlin, G., Wright, G.S., Azzollini, R., Blommaert, J.A.D.L., Brandl, B., Decin, L., Nayak, O., Royer, P., Sargent, B.A., van der Werf, P.: Imaging of I Zw 18

- by JWST. I. Detecting Dusty Stellar Populations. *Astron. J.* **168**, 23 (2024) <https://doi.org/10.3847/1538-3881/ad4967>
- [52] Lenkić, L., Nally, C., Jones, O.C., Boyer, M.L., Kavanagh, P.J., Habel, N., Nayak, O., Hirschauer, A.S., Meixner, M., Sargent, B.A., Temim, T.: A JWST/MIRI and NIRCam Analysis of the Young Stellar Object Population in the Spitzer I Region of NGC 6822. *ApJ* **967**(2), 110 (2024) <https://doi.org/10.3847/1538-4357/ad3f90>
 - [53] Nally, C., Jones, O.C., Lenkić, L., Habel, N., Hirschauer, A.S., Meixner, M., Kavanagh, P.J., Boyer, M.L., Ferguson, A.M.N., Sargent, B.A., Nayak, O., Temim, T.: JWST MIRI and NIRCam unveil previously unseen infrared stellar populations in NGC 6822. *Mon. Not. R. Astron. Soc.* **531**, 183–198 (2024) <https://doi.org/10.1093/mnras/stae1163>
 - [54] Chown, R., Leroy, A.K., Bolatto, A.D., Chastenet, J., Glover, S.C.O., Indebetouw, R., Koch, E.W., Donovan Meyer, J., Pingel, N.M., Rosolowsky, E., Sandstrom, K., Sutter, J., Tarantino, E., Bigiel, F., Boquien, M., Chiang, I.-D., Dale, D.A., Dalcanton, J.J., Egorov, O.V., Eibensteiner, C., Grasha, K., Hassani, H., He, H., Kim, J., Meidt, S., Pathak, D., Sarbadhicary, S.K., Stanimirovic, S., Villanueva, V., Williams, T.G.: Relationships between Polycyclic Aromatic Hydrocarbons, Small Dust Grains, H₂, and H I in Local Group Dwarf Galaxies NGC 6822 and WLM Using JWST, ALMA, and the VLA. *Astrophys. J.* **987**, 91 (2025) <https://doi.org/10.3847/1538-4357/add73a>
 - [55] Mingozi, M., Garcia del Valle-Espinosa, M., James, B.L., Rickards Vaught, R.J., Hayes, M., Amorín, R.O., Leitherer, C., Aloisi, A., Hunt, L., Law, D., Richardson, C.T., Pidgeon, A., Arellano-Córdova, K.Z., Berg, D.A., Chisholm, J., Hernandez, S., Jones, L., Kumari, N., Martin, C.L., Ravindranath, S., Vallini, L., Xu, X.: Exploring the Mysterious High-ionization Source Powering [Ne V] in High-z Analog SBS0335-052 E with JWST/MIRI. *Astrophys. J.* **985**, 253 (2025) <https://doi.org/10.3847/1538-4357/adc996>
 - [56] Hunt, L.K., Draine, B.T., Navarro, M.G., Aloisi, A., Vaught, R.J.R., Adamo, A., Annibali, F., Calzetti, D., Hernandez, S., James, B.L., Mingozi, M., Schneider, R., Tosi, M., Brandl, B., del Valle-Espinosa, M.G., Donnan, F., Hirschauer, A.S., Meixner, M., Rigopoulou, D.: The Interstellar Medium in I Zw 18 Seen with JWST/MIRI. II. Warm Molecular Hydrogen and Warm Dust. *Astrophys. J.* **993**, 84 (2025) <https://doi.org/10.3847/1538-4357/ae0191>
 - [57] Telford, O.G., Sandstrom, K.M., McQuinn, K.B.W., Glover, S.C.O., Tarantino, E.J., Bolatto, A.D., Rickards Vaught, R.J.: Molecular hydrogen in the extremely metal- and dust-poor galaxy Leo P. *Nature* **642**(8069), 900–904 (2025) <https://doi.org/10.1038/s41586-025-09115-7>
 - [58] Lai, T.S.-Y., Duval, S., Smith, J.D.T., Armus, L., Witt, A.N., Sandstrom, K., Tarantino, E., Baba, S., Bolatto, A., Donnelly, G.P., Hensley, B.S., Imanishi, M., Lenkić, L., Linden, S., Nakagawa, T., Spoon, H.W.W., Togi, A., Whitcomb, C.M.: Resolving Emission from Small Dust Grains in the Blue Compact Dwarf II Zw 40 with JWST. *Astrophys. J.* **991**, 56 (2025) <https://doi.org/10.3847/2041-8213/ae0467>
 - [59] Whitcomb, C.M., Smith, J.-D.T., Tarantino, E., Sandstrom, K., Lai, T.S.-Y., Armus, L., Bolatto, A., Boyer, M., Dale, D.A., Draine, B.T., Hensley, B.S., Narayanan, D., Roman-Duval, J., Skillman, E.D.: The Metallicity Dependence of PAH Emission in Galaxies II: Insights from JWST/NIRCam Imaging of the Smallest Dust Grains in M101. *arXiv* (2025). <https://ui.adsabs.harvard.edu/abs/2025arXiv250918347W>
 - [60] Kniazev, A.Y., Grebel, E.K., Pustilnik, S.A., Pramskij, A.G., Zucker, D.B.: Spectrophotometry of Sextans A and B: Chemical Abundances of H II Regions and Planetary Nebulae. *Astron. J.* **130**(4), 1558–1573 (2005) <https://doi.org/10.1086/432931>
 - [61] Asplund, M., Grevesse, N., Sauval, A.J., Scott, P.: The Chemical Composition of the Sun. *Annu. Rev. Astron. Astrophys.* **47**, 481–522 (2009) <https://doi.org/10.1146/annurev.astro.46.060407.145222>

- [62] Bellazzini, M., Beccari, G., Fraternali, F., Oosterloo, T.A., Sollima, A., Testa, V., Galletti, S., Perina, S., Faccini, M., Cusano, F.: The extended structure of the dwarf irregular galaxies Sextans A and Sextans B. Signatures of tidal distortion in the outskirts of the Local Group. *Astron. Astrophys.* **566**, 44 (2014) <https://doi.org/10.1051/0004-6361/201423659>
- [63] McQuinn, K.B.W., Boyer, M.L., Mitchell, M.B., Skillman, E.D., Gehrz, R.D., Groenewegen, M.A.T., McDonald, I., Sloan, G.C., van Loon, J.T., Whitelock, P.A., Zijlstra, A.A.: DUSTiNGS. III. Distribution of Intermediate-age and Old Stellar Populations in Disks and Outer Extremities of Dwarf Galaxies. *Astrophys. J.* **834**(1), 78 (2017) <https://doi.org/10.3847/1538-4357/834/1/78>
- [64] Ott, J., Stilp, A.M., Warren, S.R., Skillman, E.D., Dalcanton, J.J., Walter, F., de Blok, W.J.G., Koribalski, B., West, A.A.: VLA-ANGST: A High-resolution H I Survey of Nearby Dwarf Galaxies. *Astron. J.* **144**, 123 (2012) <https://doi.org/10.1088/0004-6256/144/4/123>
- [65] McConnachie, A.W.: The Observed Properties of Dwarf Galaxies in and around the Local Group. *Astron. J.* **144**, 4 (2012) <https://doi.org/10.1088/0004-6256/144/1/4>
- [66] Lee, J.C., Gil de Paz, A., Tremonti, C., Kennicutt, R.C., Salim, S., Bothwell, M., Calzetti, D., Dalcanton, J., Dale, D., Engelbracht, C., José G. Funes, S.J., Johnson, B., Sakai, S., Skillman, E., van Zee, L., Walter, F., Weisz, D.: COMPARISON OF H α AND UV STAR FORMATION RATES IN THE LOCAL VOLUME: SYSTEMATIC DISCREPANCIES FOR DWARF GALAXIES. *ApJ* **706**(1), 599 (2009) <https://doi.org/10.1088/0004-637X/706/1/599>
- [67] Shi, Y., Armus, L., Helou, G., Stierwalt, S., Gao, Y., Wang, J., Zhang, Z.-Y., Gu, Q.: Inefficient star formation in extremely metal poor galaxies. *Nature* **514**(7522), 335–338 (2014) <https://doi.org/10.1038/nature13820>
- [68] Lupton, R., Blanton, M.R., Fekete, G., Hogg, D.W., O’Mullane, W., Szalay, A., Wherry, N.: Preparing Red-Green-Blue Images from CCD Data. *Publ. Astron. Soc. Pac.* **116**, 133–137 (2004) <https://doi.org/10.1086/382245>
- [69] Draine, B.T., Li, A., Hensley, B.S., Hunt, L.K., Sandstrom, K., Smith, J.-D.T.: Excitation of Polycyclic Aromatic Hydrocarbon Emission: Dependence on Size Distribution, Ionization, and Starlight Spectrum and Intensity. *Astrophys. J.* **917**(1), 3 (2021) <https://doi.org/10.3847/1538-4357/abff51>
- [70] Husser, T.-O., Berg, S.W.-v., Dreizler, S., Homeier, D., Reiners, A., Barman, T., Hauschildt, P.H.: A new extensive library of PHOENIX stellar atmospheres and synthetic spectra. *A&A* **553**, 6 (2013) <https://doi.org/10.1051/0004-6361/201219058>
- [71] Sandstrom, K.M., Chastenet, J., Sutter, J., Leroy, A.K., Egorov, O.V., Williams, T.G., Bolatto, A.D., Boquien, M., Cao, Y., Dale, D.A., Lee, J.C., Rosolowsky, E., Schinnerer, E., Barnes, Ashley.T., Belfiore, F., Bigiel, F., Chevance, M., Grasha, K., Groves, B., Hassani, H., Hughes, A., Klessen, R.S., Kruijssen, J.M.D., Larson, K.L., Liu, D., Lopez, L.A., Meidt, S.E., Murphy, E.J., Sormani, M.C., Thilker, D.A., Watkins, E.J.: PHANGS-JWST First Results: Mapping the 3.3 μ m Polycyclic Aromatic Hydrocarbon Vibrational Band in Nearby Galaxies with NIRC2 Medium Bands. *Astrophys. J. Lett.* **944**(2), 7 (2023) <https://doi.org/10.3847/2041-8213/acb0cf>
- [72] Kennicutt, R.C. Jr., Lee, J.C., Funes, J.G., J., S., Sakai, S., Akiyama, S.: An H α Imaging Survey of Galaxies in the Local 11 Mpc Volume. *Astrophys. J. Suppl. Ser.* **178**, 247–279 (2008) <https://doi.org/10.1086/590058>
- [73] Lorenzo, M., Garcia, M., Najarro, F., Herrero, A., Cerviño, M., Castro, N.: A new reference catalogue for the very metal-poor Universe: +150 OB stars in Sextans A. *Mon. Not. R. Astron. Soc.* **516**(3), 4164–4179 (2022) <https://doi.org/10.1093/mnras/stac2050>
- [74] Sandstrom, K.M., Koch, E.W., Leroy, A.K., Rosolowsky, E., Emsellem, E., Smith, R.J., Egorov,

- O.V., Williams, T.G., Larson, K.L., Lee, J.C., Schinnerer, E., Thilker, D.A., Barnes, A.T., Belfiore, F., Bigiel, F., Blanc, G.A., Bolatto, A.D., Boquien, M., Cao, Y., Chastenet, J., Chevance, M., Chiang, I.-D., Dale, D.A., Faesi, C.M., Glover, S.C.O., Grasha, K., Groves, B., Hassani, H., Henshaw, J.D., Hughes, A., Kim, J., Klessen, R.S., Kreckel, K., Kruijssen, J.M.D., Lopez, L.A., Liu, D., Meidt, S.E., Murphy, E.J., Pan, H.-A., Querejeta, M., Saito, T., Sardone, A., Sormani, M.C., Sutter, J., Usero, A., Watkins, E.J.: PHANGS-JWST First Results: Tracing the Diffuse Interstellar Medium with JWST Imaging of Polycyclic Aromatic Hydrocarbon Emission in Nearby Galaxies. *Astrophys. J. Lett.* **944**(2), 8 (2023) <https://doi.org/10.3847/2041-8213/aca972>
- [75] Thilker, D.A., Lee, J.C., Deger, S., Barnes, A.T., Bigiel, F., Boquien, M., Cao, Y., Chevance, M., Dale, D.A., Egorov, O.V., Glover, S.C.O., Grasha, K., Henshaw, J.D., Klessen, R.S., Koch, E., Kruijssen, J.M.D., Leroy, A.K., Lessing, R.A., Meidt, S.E., Pinna, F., Querejeta, M., Rosolowsky, E., Sandstrom, K.M., Schinnerer, E., Smith, R.J., Watkins, E.J., Williams, T.G., Anand, G.S., Belfiore, F., Blanc, G.A., Chandar, R., Congiu, E., Emsellem, E., Groves, B., Kreckel, K., Larson, K.L., Liu, D., Pessa, I., Whitmore, B.C.: PHANGS-JWST First Results: The Dust Filament Network of NGC 628 and Its Relation to Star Formation Activity. *Astrophys. J.* **944**, 13 (2023) <https://doi.org/10.3847/2041-8213/acaec>
- [76] Sutter, J., Sandstrom, K., Chastenet, J., Leroy, A.K., Koch, E.W., Williams, T.G., Chown, R., Belfiore, F., Bigiel, F., Boquien, M., Cao, Y., Chevance, M., Dale, D.A., Egorov, O.V., Glover, S.C.O., Groves, B., Klessen, R.S., Kreckel, K., Larson, K.L., Oakes, E.K., Pathak, D., Ramambason, L., Rosolowsky, E., Watkins, E.J.: The Fraction of Dust Mass in the Form of Polycyclic Aromatic Hydrocarbons on 10–50 pc Scales in Nearby Galaxies. *Astrophys. J.* **971**(2), 178 (2024) <https://doi.org/10.3847/1538-4357/ad54bd>
- [77] Russell, S.C., Dopita, M.A.: Abundances of the Heavy Elements in the Magellanic Clouds. III. Interpretation of Results. *Astrophys. J.* **384**, 508 (1992) <https://doi.org/10.1086/170893>
- [78] Clark, I.Y., Sandstrom, K., Wolfire, M., Bolatto, A.D., Chastenet, J., Dale, D.A., Gaches, B.A.L., Glover, S.C.O., Goicoechea, J.R., Gordon, K.D., Groves, B., Hands, L., Klessen, R., De Looze, I., Smith, J.D.T., Van De Putte, D., Walch, S.K.: The Resolved Structure of a Low-metallicity Photodissociation Region. *Astrophys. J.* **990**, 209 (2025) <https://doi.org/10.3847/1538-4357/ade38>
- [79] Rubio, M., Elmegreen, B.G., Hunter, D.A., Brinks, E., Cortés, J.R., Cigan, P.: Dense cloud cores revealed by CO in the low metallicity dwarf galaxy WLM. *Nature* **525**(7568), 218–221 (2015) <https://doi.org/10.1038/nature14901>
- [80] Elmegreen, B.G., Rubio, M., Hunter, D.A., Verdugo, C., Brinks, E., Schrubba, A.: Carbon monoxide in clouds at low metallicity in the dwarf irregular galaxy WLM. *Nature* **495**(7442), 487–489 (2013) <https://doi.org/10.1038/nature11933>
- [81] Schrubba, A., Leroy, A.K., Kruijssen, J.M.D., Bigiel, F., Bolatto, A.D., de Blok, W.J.G., Tacconi, L., van Dishoeck, E.F., Walter, F.: Physical Properties of Molecular Clouds at 2 pc Resolution in the Low-metallicity Dwarf Galaxy NGC 6822 and the Milky Way. *Astrophys. J.* **835**(2), 278 (2017) <https://doi.org/10.3847/1538-4357/835/2/278>
- [82] Shi, Y., Wang, J., Zhang, Z.-Y., Zhang, Q., Gao, Y., Zhou, L., Gu, Q., Qiu, K., Xia, X.-Y., Hao, C.-N., Chen, Y.: Oversized Gas Clumps in an Extremely Metal-poor Molecular Cloud Revealed by ALMA’s Parsec-scale Maps. *Astrophys. J.* **892**(2), 147 (2020) <https://doi.org/10.3847/1538-4357/ab7a12>
- [83] De Vis, P., Jones, A., Viaene, S., Casasola, V., Clark, C.J.R., Baes, M., Bianchi, S., Cassara, L.P., Davies, J.I., De Looze, I., Galametz, M., Galliano, F., Lianou, S., Madden, S., Manilla-Robles, A., Mosenkov, A.V., Nersesian, A., Roychowdhury, S., Xilouris, E.M., Ysard, N.: A systematic metallicity study of DustPedia galaxies reveals evolution in the dust-to-metal ratios. *Astron. Astrophys.* **623**, 5 (2019) <https://doi.org/10.1051/0004-6361/201834444>

- [84] Hamanowicz, A., Tchernyshyov, K., Roman-Duval, J., Jenkins, E.B., Rafelski, M., Gordon, K.D., Zheng, Y., Garcia, M., Werk, J.: METAL-Z: Measuring Dust Depletion in Low-metallicity Dwarf Galaxies. *Astrophys. J.* **966**, 80 (2024) <https://doi.org/10.3847/1538-4357/ad307b>
- [85] Bolatto, A.D., Jackson, J.M., Ingalls, J.G.: A Semianalytical Model for the Observational Properties of the Dominant Carbon Species at Different Metallicities. *Astrophys. J.* **513**, 275–286 (1999) <https://doi.org/10.1086/306849>
- [86] Wolfire, M.G., Hollenbach, D., McKee, C.F.: The Dark Molecular Gas. *Astrophys. J.* **716**(2), 1191–1207 (2010) <https://doi.org/10.1088/0004-637X/716/2/1191>
- [87] Madden, S.C., Cormier, D., Hony, S., Lebouteiller, V., Abel, N., Galametz, M., De Looze, I., Chevance, M., Polles, F.L., Lee, M.-Y., Galliano, F., Lambert-Huyghe, A., Hu, D., Ramambason, L.: Tracing the total molecular gas in galaxies: [CII] and the CO-dark gas. *Astron. Astrophys.* **643**, 141 (2020) <https://doi.org/10.1051/0004-6361/202038860>
- [88] Kennicutt, R.C. Jr., Armus, L., Bendo, G., Calzetti, D., Dale, D.A., Draine, B.T., Engelbracht, C.W., Gordon, K.D., Grauer, A.D., Helou, G., Hollenbach, D.J., Jarrett, T.H., Kewley, L.J., Leitherer, C., Li, A., Malhotra, S., Regan, M.W., Rieke, G.H., Rieke, M.J., Roussel, H., Smith, J.-D.T., Thornley, M.D., Walter, F.: SINGS: The SIRTf Nearby Galaxies Survey. *Publ. Astron. Soc. Pac.* **115**, 928–952 (2003) <https://doi.org/10.1086/376941>
- [89] Chastenet, J., Sutter, J., Sandstrom, K., Belfiore, F., Egorov, O.V., Larson, K.L., Leroy, A.K., Liu, D., Rosolowsky, E., Thilker, D.A., Watkins, E.J., Williams, T.G., Barnes, Ashley.T., Bigiel, F., Boquien, M., Chevance, M., Chiang, I.-D., Dale, D.A., Kruijssen, J.M.D., Emsellem, E., Grasha, K., Groves, B., Hassani, H., Hughes, A., Kreckel, K., Meidt, S.E., Rickards Vaught, R.J., Sardone, A., Schinnerer, E.: PHANGS-JWST First Results: Variations in PAH Fraction as a Function of ISM Phase and Metallicity. *Astrophys. J. Lett.* **944**(2), 11 (2023) <https://doi.org/10.3847/2041-8213/acadd7>
- [90] Egorov, O.V., Kreckel, K., Sandstrom, K.M., Leroy, A.K., Glover, S.C.O., Groves, B., Kruijssen, J.M.D., Barnes, Ashley.T., Belfiore, F., Bigiel, F., Blanc, G.A., Boquien, M., Cao, Y., Chastenet, J., Chevance, M., Congiu, E., Dale, D.A., Emsellem, E., Grasha, K., Klessen, R.S., Larson, K.L., Liu, D., Murphy, E.J., Pan, H.-A., Pessa, I., Pety, J., Rosolowsky, E., Scheuermann, F., Schinnerer, E., Sutter, J., Thilker, D.A., Watkins, E.J., Williams, T.G.: PHANGS-JWST First Results: Destruction of the PAH Molecules in H II Regions Probed by JWST and MUSE. *Astrophys. J. Lett.* **944**(2), 16 (2023) <https://doi.org/10.3847/2041-8213/acac92>
- [91] Egorov, O.V., Leroy, A.K., Sandstrom, K., Kreckel, K., Baron, D., Belfiore, F., Chown, R., Sutter, J., Boquien, M., Saguer, M.C., Congiu, E., Dale, D.A., Egorova, E., Huber, M., Li, J., Williams, T.G., Chastenet, J., Chiang, I.-D., Gerasimov, I., Hassani, H., Kim, H., Koziol, H., Lee, J.C., McClain, R.L., Méndez Delgado, J.E., Pan, H.-A., Pathak, D., Rosolowsky, E., Sarbadhicary, S.K., Schinnerer, E., Thilker, D., Ubeda, L., Weinbeck, T.: Polycyclic Aromatic Hydrocarbons Destruction in Star-Forming Regions across 42 Nearby Galaxies. *arXiv* (2025). <https://ui.adsabs.harvard.edu/abs/2025arXiv250913845E>
- [92] Allamandola, L.J., Hudgins, D.M., Sandford, S.A.: Modeling the Unidentified Infrared Emission with Combinations of Polycyclic Aromatic Hydrocarbons. *Astrophys. J.* **511**, 115–119 (1999) <https://doi.org/10.1086/311843>
- [93] Hudgins, D.M., Allamandola, L.J.: The Spacing of the Interstellar 6.2 and 7.7 Micron Emission Features as an Indicator of Polycyclic Aromatic Hydrocarbon Size. *Astrophys. J.* **513**, 69–73 (1999) <https://doi.org/10.1086/311901>
- [94] Bauschlicher, C.W. Jr., Peeters, E., Allamandola, L.J.: The Infrared Spectra of Very Large, Compact, Highly Symmetric, Polycyclic Aromatic Hydrocarbons (PAHs). *Astrophys. J.* **678**, 316–327 (2008) <https://doi.org/10.1086/533424>

- [95] Shannon, M.J., Boersma, C.: Examining the Class B to A Shift of the 7.7 *Mm* PAH Band with the NASA Ames PAH IR Spectroscopic Database. *Astrophys. J.* **871**, 124 (2019) <https://doi.org/10.3847/1538-4357/aaf562>
- [96] Maragkoudakis, A., Peeters, E., Ricca, A., Boersma, C.: Polycyclic aromatic hydrocarbon size tracers. *Mon. Not. R. Astron. Soc.* **524**, 3429–3436 (2023) <https://doi.org/10.1093/mnras/stad2062>
- [97] Schutte, W.A., Tielens, A.G.G.M., Allamandola, L.J.: Theoretical Modeling of the Infrared Fluorescence from Interstellar Polycyclic Aromatic Hydrocarbons. *Astrophys. J.* **415**, 397 (1993) <https://doi.org/10.1086/173173>
- [98] Maragkoudakis, A., Peeters, E., Ricca, A.: Probing the size and charge of polycyclic aromatic hydrocarbons. *Mon. Not. R. Astron. Soc.* **494**, 642–664 (2020) <https://doi.org/10.1093/mnras/staa681>
- [99] Dale, D.A., Cohen, S.A., Johnson, L.C., Schuster, M.D., Calzetti, D., Engelbracht, C.W., Gil de Paz, A., Kennicutt, R.C., Lee, J.C., Begum, A., Block, M., Dalcanton, J.J., Funes, J.G., Gordon, K.D., Johnson, B.D., Marble, A.R., Sakai, S., Skillman, E.D., van Zee, L., Walter, F., Weisz, D.R., Williams, B., Wu, S.-Y., Wu, Y.: The Spitzer Local Volume Legacy: Survey Description and Infrared Photometry. *Astrophys. J.* **703**, 517–556 (2009) <https://doi.org/10.1088/0004-637X/703/1/517>
- [100] Bruzual, G., Charlot, S.: Stellar population synthesis at the resolution of 2003. *Mon. Not. R. Astron. Soc.* **344**, 1000–1028 (2003) <https://doi.org/10.1046/j.1365-8711.2003.06897.x>
- [101] Draine, B.T., Li, A.: Infrared Emission from Interstellar Dust. IV. The Silicate-Graphite-PAH Model in the Post-Spitzer Era. *Astrophys. J.* **657**, 810–837 (2007) <https://doi.org/10.1086/511055>
- [102] Chown, R., Sidhu, A., Peeters, E., Tielens, A.G.G.M., Cami, J., Berné, O., Habart, E., Alarcón, F., Canin, A., Schroetter, I., Trahin, B., Van De Putte, D., Abergel, A., Bergin, E.A., Bernard-Salas, J., Boersma, C., Bron, E., Cuadrado, S., Dartois, E., Dicken, D., El-Yajouri, M., Fuente, A., Goicoechea, J.R., Gordon, K.D., Issa, L., Joblin, C., Kannavou, O., Khan, B., Lacinbala, O., Languignon, D., Le Gal, R., Maragkoudakis, A., Meshaka, R., Okada, Y., Onaka, T., Pasquini, S., Pound, M.W., Robberto, M., Röllig, M., Schefter, B., Schirmer, T., Vicente, S., Wolfire, M.G., Zannese, M., Aleman, I., Allamandola, L., Auchettl, R., Baratta, G.A., Bejaoui, S., Bera, P.P., Black, J.H., Boulanger, F., Bouwman, J., Brandl, B., Brechignac, P., Brünken, S., Buragohain, M., Burkhardt, A., Candian, A., Cazaux, S., Cernicharo, J., Chabot, M., Chakraborty, S., Champion, J., Colgan, S.W.J., Cooke, I.R., Coutens, A., Cox, N.L.J., Demyk, K., Meyer, J.D., Foschino, S., García-Lario, P., Gavilan, L., Gerin, M., Gottlieb, C.A., Guillard, P., Gusdorf, A., Hartigan, P., He, J., Herbst, E., Hornekaer, L., Jäger, C., Janot-Pacheco, E., Kaufman, M., Kemper, F., Kendrew, S., Kirsanova, M.S., Klaassen, P., Kwok, S., Labiano, Á., Lai, T.S.-Y., Lee, T.J., Lefloch, B., Le Petit, F., Li, A., Linz, H., Mackie, C.J., Madden, S.C., Mascetti, J., McGuire, B.A., Merino, P., Micelotta, E.R., Misselt, K., Morse, J.A., Mulas, G., Neelamkodan, N., Ohsawa, R., Omont, A., Paladini, R., Palumbo, M.E., Pathak, A., Pendleton, Y.J., Petrignani, A., Pino, T., Puga, E., Rangwala, N., Rapacioli, M., Ricca, A., Roman-Duval, J., Roser, J., Roueff, E., Rouillé, G., Salama, F., Sales, D.A., Sandstrom, K., Sarre, P., Sciamma-O’Brien, E., Sellgren, K., Shenoy, S.S., Teyssier, D., Thomas, R.D., Togi, A., Verstraete, L., Witt, A.N., Wootten, A., Zettergren, H., Zhang, Y., Zhang, Z.E., Zhen, J.: PDRs4All. IV. An embarrassment of riches: Aromatic infrared bands in the Orion Bar. *Astron. Astrophys.* **685**, 75 (2024) <https://doi.org/10.1051/0004-6361/202346662>
- [103] Van De Putte, D., Meshaka, R., Trahin, B., Habart, E., Peeters, E., Berné, O., Alarcón, F., Canin, A., Chown, R., Schroetter, I., Sidhu, A., Boersma, C., Bron, E., Dartois, E., Goicoechea, J.R., Gordon, K.D., Onaka, T., Tielens, A.G.G.M., Verstraete, L., Wolfire, M.G., Abergel, A., Bergin, E.A., Bernard-Salas, J., Cami, J., Cuadrado, S., Dicken, D., Elyajouri, M., Fuente, A., Joblin, C., Khan, B., Lacinbala, O., Languignon, D., Le Gal, R., Maragkoudakis, A., Okada, Y., Pasquini, S., Pound, M.W., Robberto, M., Röllig, M., Schefter, B., Schirmer, T., Tabone, B., Vicente, S., Zannese, M., Colgan, S.W.J., He, J., Rouillé, G., Togi, A., Aleman, I., Auchettl, R., Baratta, G.A., Bejaoui, S., Bera, P.P., Black, J.H., Boulanger, F., Bouwman, J., Brandl, B., Brechignac,

- P., Brünken, S., Buragohain, M., Burkhardt, A., Candian, A., Cazaux, S., Cernicharo, J., Chabot, M., Chakraborty, S., Champion, J., Cooke, I.R., Coutens, A., Cox, N.L.J., Demyk, K., Meyer, J.D., Foschino, S., García-Lario, P., Gerin, M., Gottlieb, C.A., Guillard, P., Gusdorf, A., Hartigan, P., Herbst, E., Hornekaer, L., Issa, L., Jäger, C., Janot-Pacheco, E., Kannavou, O., Kaufman, M., Kemper, F., Kendrew, S., Kirsanova, M.S., Klaassen, P., Kwok, S., Labiano, Á., Lai, T.S.-Y., Le Floch, B., Le Petit, F., Li, A., Linz, H., Mackie, C.J., Madden, S.C., Mascetti, J., McGuire, B.A., Merino, P., Micelotta, E.R., Morse, J.A., Mulas, G., Neelamkodan, N., Ohsawa, R., Omont, A., Paladini, R., Palumbo, M.E., Pathak, A., Pendleton, Y.J., Petrignani, A., Pino, T., Puga, E., Rangwala, N., Rapacioli, M., Rho, J., Ricca, A., Roman-Duval, J., Roser, J., Roueff, E., Salama, F., Sales, D.A., Sandstrom, K., Sarre, P., Sciamma-O'Brien, E., Sellgren, K., Shenoy, S.S., Teyssier, D., Thomas, R.D., Witt, A.N., Wootten, A., Ysard, N., Zettergren, H., Zhang, Y., Zhang, Z.E., Zhen, J.: PDRs4All: VIII. Mid-infrared emission line inventory of the Orion Bar. *A&A* **687**, 86 (2024) <https://doi.org/10.1051/0004-6361/202449295>
- [104] Peeters, E., Habart, E., Berné, O., Sidhu, A., Chown, R., Van De Putte, D., Trahin, B., Schroetter, I., Canin, A., Alarcón, F., Schefter, B., Khan, B., Pasquini, S., Tielens, A.G.G.M., Wolfire, M.G., Dartois, E., Goicoechea, J.R., Maragkoudakis, A., Onaka, T., Pound, M.W., Vicente, S., Abergel, A., Bergin, E.A., Bernard-Salas, J., Boersma, C., Bron, E., Cami, J., Cuadrado, S., Dicken, D., Elyajouri, M., Fuente, A., Gordon, K.D., Issa, L., Joblin, C., Kannavou, O., Lacinbala, O., Languignon, D., Le Gal, R., Meshaka, R., Okada, Y., Robberto, M., Röllig, M., Schirmer, T., Tabone, B., Zannese, M., Aleman, I., Allamandola, L., Auchettl, R., Baratta, G.A., Bejaoui, S., Bera, P.P., Black, J.H., Boulanger, F., Bouwman, J., Brandl, B., Brechignac, P., Brünken, S., Buragohain, M., Burkhardt, A., Candian, A., Cazaux, S., Cernicharo, J., Chabot, M., Chakraborty, S., Champion, J., Colgan, S.W.J., Cooke, I.R., Coutens, A., Cox, N.L.J., Demyk, K., Meyer, J.D., Foschino, S., García-Lario, P., Gerin, M., Gottlieb, C.A., Guillard, P., Gusdorf, A., Hartigan, P., He, J., Herbst, E., Hornekaer, L., Jäger, C., Janot-Pacheco, E., Kaufman, M., Kendrew, S., Kirsanova, M.S., Klaassen, P., Kwok, S., Labiano, Á., Lai, T.S.-Y., Lee, T.J., Lefloch, B., Le Petit, F., Li, A., Linz, H., Mackie, C.J., Madden, S.C., Mascetti, J., McGuire, B.A., Merino, P., Micelotta, E.R., Misselt, K., Morse, J.A., Mulas, G., Neelamkodan, N., Ohsawa, R., Paladini, R., Palumbo, M.E., Pathak, A., Pendleton, Y.J., Petrignani, A., Pino, T., Puga, E., Rangwala, N., Rapacioli, M., Ricca, A., Roman-Duval, J., Roser, J., Roueff, E., Rouillé, G., Salama, F., Sales, D.A., Sandstrom, K., Sarre, P., Sciamma-O'Brien, E., Sellgren, K., Shenoy, S.S., Teyssier, D., Thomas, R.D., Togi, A., Verstraete, L., Witt, A.N., Wootten, A., Ysard, N., Zettergren, H., Zhang, Y., Zhang, Z.E., Zhen, J.: PDRs4All: III. JWST's NIR spectroscopic view of the Orion Bar. *Astron. Astrophys.* **685**, 74 (2024) <https://doi.org/10.1051/0004-6361/202348244>
- [105] Van De Putte, D., Peeters, E., Gordon, K.D., Smith, J.-D.T., Lai, T.S.-Y., Maragkoudakis, A., Schefter, B., Sidhu, A., Doshi, D., Berné, O., Cami, J., Boersma, C., Dartois, E., Habart, E., Onaka, T., Tielens, A.G.G.M.: PDRs4All: XVI. Tracing aromatic infrared band characteristics in photodissociation region spectra with PAHFIT in the JWST era. *Astron. Astrophys.* **701**, 111 (2025) <https://doi.org/10.1051/0004-6361/202554991>
- [106] Lai, T.S.-Y., Smith, J.D.T., Baba, S., Spoon, H.W.W., Imanishi, M.: All the PAHs: An AKARI-Spitzer Cross-archival Spectroscopic Survey of Aromatic Emission in Galaxies. *Astrophys. J.* **905**(1), 55 (2020) <https://doi.org/10.3847/1538-4357/abc002>
- [107] Zhang, C., Hales, J., Peeters, E., Cami, J., Sidhu, A., Zhen, J.: A JWST Study of Polycyclic Aromatic Hydrocarbon Emission in a Region of 30 Doradus. *Astrophys. J. Suppl. Ser.* **280**, 4 (2025) <https://doi.org/10.3847/1538-4365/adea6b>
- [108] Hunter, D.A., Zahedy, F., Bowsher, E.C., Wilcots, E.M., Kepley, A.A., Gaal, V.: Mapping the Extended H I Distribution of Three Dwarf Galaxies. *Astron. J.* **142**, 173 (2011) <https://doi.org/10.1088/0004-6256/142/5/173>
- [109] Dale, D.A., Graham, G.B., Barnes, A.T., Baron, D., Bigiel, F., Boquien, M., Chandar, R., Chasstenet, J., Chown, R., Egorov, O.V., Glover, S.C.O., Hands, L., Henny, K.F., Indebetouw, R.,

- Klessen, R.S., Larson, K.L., Lee, J.C., Leroy, A.K., Maschmann, D., Pathak, D., Rodríguez, M.J., Rosolowsky, E., Sandstrom, K., Schinnerer, E., Sutter, J., Thilker, D.A., Weinbeck, T.D., Whitmore, B.C., Williams, T.G., Wofford, A.: PAH Feature Ratios around Stellar Clusters and Associations in 19 Nearby Galaxies. *Astron. J.* **169**, 133 (2025) <https://doi.org/10.3847/1538-3881/ada89f>
- [110] McGuire, B.A., Burkhardt, A.M., Kalenskii, S., Shingledecker, C.N., Remijan, A.J., Herbst, E., McCarthy, M.C.: Detection of the aromatic molecule benzonitrile ($c\text{-C}_6\text{H}_5\text{CN}$) in the interstellar medium. *Science* **359**, 202–205 (2018) <https://doi.org/10.1126/science.aao4890>
- [111] Lemmens, A.K., Rap, D.B., Thunnissen, J.M.M., Willemsen, B., Rijs, A.M.: Polycyclic aromatic hydrocarbon formation chemistry in a plasma jet revealed by IR-UV action spectroscopy. *Nat. Commun.* **11**, 269 (2020) <https://doi.org/10.1038/s41467-019-14092-3>
- [112] McGuire, B.A., Loomis, R.A., Burkhardt, A.M., Lee, K.L.K., Shingledecker, C.N., Charnley, S.B., Cooke, I.R., Cordiner, M.A., Herbst, E., Kalenskii, S., Siebert, M.A., Willis, E.R., Xue, C., Remijan, A.J., McCarthy, M.C.: Detection of two interstellar polycyclic aromatic hydrocarbons via spectral matched filtering. *Sci. Vol. 371 Issue 6535 Pp 1265-1269 2021* **371**(6535), 1265 (2021) <https://doi.org/10.1126/science.abb7535>
- [113] Burkhardt, A.M., Long Kelvin Lee, K., Bryan Changala, P., Shingledecker, C.N., Cooke, I.R., Loomis, R.A., Wei, H., Charnley, S.B., Herbst, E., McCarthy, M.C., McGuire, B.A.: Discovery of the Pure Polycyclic Aromatic Hydrocarbon Indene ($c\text{-C}_9\text{H}_8$) with GOTHAM Observations of TMC-1. *ApJL* **913**(2), 18 (2021) <https://doi.org/10.3847/2041-8213/abfd3a>
- [114] Wenzel, G., Cooke, I.R., Changala, P.B., Bergin, E.A., Zhang, S., Burkhardt, A.M., Byrne, A.N., Charnley, S.B., Cordiner, M.A., Duffy, M., Fried, Z.T.P., Gupta, H., Holdren, M.S., Lipnicky, A., Loomis, R.A., Shay, H.T., Shingledecker, C.N., Siebert, M.A., Stewart, D.A., Willis, R.H.J., Xue, C., Remijan, A.J., Wendlandt, A.E., McCarthy, M.C., McGuire, B.A.: Detection of interstellar 1-cyanopyrene: A four-ring polycyclic aromatic hydrocarbon. *Science* **386**, 810–813 (2024) <https://doi.org/10.1126/science.adq6391>
- [115] Zhang, X., Hensley, B.S., Green, G.M.: Dust-extinction-curve Variation in the Translucent Interstellar Medium Is Driven by Polycyclic Aromatic Hydrocarbon Growth. *Astrophys. J.* **979**, 17 (2025) <https://doi.org/10.3847/2041-8213/ada28f>
- [116] Allain, T., Leach, S., Sedlmayr, E.: Photodestruction of PAHs in the interstellar medium. II. Influence of the states of ionization and hydrogenation. *Astron. Astrophys.* **305**, 616 (1996)
- [117] Allain, T., Leach, S., Sedlmayr, E.: Photodestruction of PAHs in the interstellar medium. I. Photodissociation rates for the loss of an acetylenic group. *Astron. Astrophys.* **305**, 602 (1996)
- [118] Micelotta, E.R., Jones, A.P., Tielens, A.G.G.M.: Polycyclic aromatic hydrocarbon processing by cosmic rays. *Astron. Astrophys.* **526**, 52 (2011) <https://doi.org/10.1051/0004-6361/201015741>
- [119] Gardner, J.P., Mather, J.C., Clampin, M., Doyon, R., Greenhouse, M.A., Hammel, H.B., Hutchings, J.B., Jakobsen, P., Lilly, S.J., Long, K.S., Lunine, J.I., McCaughrean, M.J., Mountain, M., Nella, J., Rieke, G.H., Rieke, M.J., Rix, H.-W., Smith, E.P., Sonneborn, G., Stiavelli, M., Stockman, H.S., Windhorst, R.A., Wright, G.S.: The James Webb Space Telescope. *Space Sci. Rev.* **123**, 485–606 (2006) <https://doi.org/10.1007/s11214-006-8315-7>
- [120] Rigby, J., Perrin, M., McElwain, M., Kimble, R., Friedman, S., Lallo, M., Doyon, R., Feinberg, L., Ferruit, P., Glasse, A., Rieke, M., Rieke, G., Wright, G., Willott, C., Colon, K., Milam, S., Neff, S., Stark, C., Valenti, J., Abell, J., Abney, F., Abul-Huda, Y., Acton, D.S., Adams, E., Adler, D., Aguilar, J., Ahmed, N., Albert, L., Alberts, S., Aldridge, D., Allen, M., Altenburg, M., Álvarez-Márquez, J., Alves de Oliveira, C., Andersen, G., Anderson, H., Anderson, S., Argyriou, I., Armstrong, A., Arribas, S., Artigau, E., Arvai, A., Atkinson, C., Bacon, G., Bair, T., Banks,

- K., Barrientes, J., Barringer, B., Bartosik, P., Bast, W., Baudoz, P., Beatty, T., Bechtold, K., Beck, T., Bergeron, E., Bergkoetter, M., Bhatawdekar, R., Birkmann, S., Blazek, R., Blome, C., Boccaletti, A., Böker, T., Boia, J., Bonaventura, N., Bond, N., Bosley, K., Boucarut, R., Bourque, M., Bouwman, J., Bower, G., Bowers, C., Boyer, M., Bradley, L., Brady, G., Braun, H., Breda, D., Bresnahan, P., Bright, S., Britt, C., Bromenschenkel, A., Brooks, B., Brooks, K., Brown, B., Brown, M., Brown, P., Bunker, A., Burger, M., Bushouse, H., Cale, S., Cameron, A., Cameron, P., Canipe, A., Caplinger, J., Caputo, F., Cara, M., Carey, L., Carniani, S., Carrasquilla, M., Carruthers, M., Case, M., Catherine, R., Chance, D., Chapman, G., Charlot, S., Charlow, B., Chayer, P., Chen, B., Cherinka, B., Chichester, S., Chilton, Z., Chonis, T., Clampin, M., Clark, C., Clark, K., Coe, D., Coleman, B., Comber, B., Comeau, T., Connolly, D., Cooper, J., Cooper, R., Coppock, E., Correnti, M., Cossou, C., Coulais, A., Coyle, L., Cracraft, M., Curti, M., Cuturic, S., Davis, K., Davis, M., Dean, B., DeLisa, A., deMeester, W., Dencheva, N., Dencheva, N., DePasquale, J., Deschenes, J., Hunor Detre, Ö., Diaz, R., Dicken, D., DiFelice, A., Dillman, M., Dixon, W., Doggett, J., Donaldson, T., Douglas, R., DuPrie, K., Dupuis, J., Durning, J., Easmin, N., Eck, W., Edeani, C., Egami, E., Ehrenwinkler, R., Eisenhamer, J., Eisenhower, M., Elie, M., Elliott, J., Elliott, K., Ellis, T., Engesser, M., Espinoza, N., Etienne, O., Etxaluze, M., Falini, P., Feeney, M., Ferry, M., Filippazzo, J., Fincham, B., Fix, M., Flagey, N., Florian, M., Flynn, J., Fontanella, E., Ford, T., Forshay, P., Fox, O., Franz, D., Fu, H., Fullerton, A., Galkin, S., Galyer, A., García Marín, M., Gardner, J.P., Gardner, L., Garland, D., Garrett, B., Gasman, D., Gaspar, A., Gaudreau, D., Gauthier, P., Geers, V., Geithner, P., Gennaro, M., Giardino, G., Girard, J., Giuliano, M., Glassmire, K., Glauser, A.: The Science Performance of JWST as Characterized in Commissioning. *Publ. Astron. Soc. Pac.* **135**, 048001 (2023) <https://doi.org/10.1088/1538-3873/acb293>
- [121] Rieke, M.J., Kelly, D., Horner, S.: Overview of James Webb Space Telescope and NIRCам’s Role. In: *Cryogenic Optical Systems and Instruments XI*, vol. 5904, pp. 1–8 (2005). <https://doi.org/10.1117/12.615554> . <https://ui.adsabs.harvard.edu/abs/2005SPIE.5904....1R>
- [122] Rieke, M.J., Kelly, D.M., Misselt, K., Stansberry, J., Boyer, M., Beatty, T., Egami, E., Florian, M., Greene, T.P., Hainline, K., Leisenring, J., Roellig, T., Schlawin, E., Sun, F., Tinnin, L., Williams, C.C., Willmer, C.N.A., Wilson, D., Clark, C.R., Rohrbach, S., Brooks, B., Canipe, A., Correnti, M., DiFelice, A., Gennaro, M., Girard, J.H., Hartig, G., Hilbert, B., Koekemoer, A.M., Nikolov, N.K., Pirzkal, N., Rest, A., Robberto, M., Sunnquist, B., Telfer, R., Wu, C.R., Ferry, M., Lewis, D., Baum, S., Beichman, C., Doyon, R., Dressler, A., Eisenstein, D.J., Ferrarese, L., Hodapp, K., Horner, S., Jaffe, D.T., Johnstone, D., Krist, J., Martin, P., McCarthy, D.W., Meyer, M., Rieke, G.H., Trauger, J., Young, E.T.: Performance of NIRCам on JWST in Flight. *Publ. Astron. Soc. Pac.* **135**, 028001 (2023) <https://doi.org/10.1088/1538-3873/acac53>
- [123] Rieke, G.H., Wright, G.S., Böker, T., Bouwman, J., Colina, L., Glasse, A., Gordon, K.D., Greene, T.P., Güdel, M., Henning, Th., Justtanont, K., Lagage, P.-O., Meixner, M.E., Nørgaard-Nielsen, H.-U., Ray, T.P., Ressler, M.E., van Dishoeck, E.F., Waelkens, C.: The Mid-Infrared Instrument for the James Webb Space Telescope, I: Introduction. *Publ. Astron. Soc. Pac.* **127**(953), 584 (2015) <https://doi.org/10.1086/682252>
- [124] Wright, G.S., Rieke, G.H., Glasse, A., Ressler, M., García Marín, M., Aguilar, J., Alberts, S., Álvarez-Márquez, J., Argyriou, I., Banks, K., Baudoz, P., Boccaletti, A., Bouchet, P., Bouwman, J., Brandl, B.R., Breda, D., Bright, S., Cale, S., Colina, L., Cossou, C., Coulais, A., Cracraft, M., De Meester, W., Dicken, D., Engesser, M., Etxaluze, M., Fox, O.D., Friedman, S., Fu, H., Gasman, D., Gáspár, A., Gastaud, R., Geers, V., Glauser, A.M., Gordon, K.D., Greene, T., Greve, T.R., Grundy, T., Güdel, M., Guillard, P., Haderlein, P., Hashimoto, R., Henning, T., Hines, D., Holler, B., Detre, Ö.H., Jahromi, A., James, B., Jones, O.C., Justtanont, K., Kavanagh, P., Kendrew, S., Klaassen, P., Krause, O., Labiano, A., Lagage, P.-O., Lambros, S., Larson, K., Law, D., Lee, D., Libralato, M., Alvez, J.L., Meixner, M., Morrison, J., Mueller, M., Murray, K., Mycroft, M., Myers, R., Nayak, O., Naylor, B., Nickson, B., Noriega-Crespo, A., Östlin, G., O’Sullivan, B., Ottens, R., Patapis, P., Penanen, K., Pietraszkiewicz, M., Ray, T., Regan, M., Roteliuk, A., Royer, P., Samara-Ratna, P., Samuelson, B., Sargent, B.A., Scheithauer, S., Schneider, A., Schreiber, J., Shaughnessy, B., Sheehan, E., Shivaiei, I., Sloan, G.C., Tamas, L., Teague, K., Temim, T., Tikkanen,

- T., Tustain, S., van Dishoeck, E.F., Vandenbussche, B., Weilert, M., Whitehouse, P., Wolff, S.: The Mid-infrared Instrument for JWST and Its In-flight Performance. *PASP* **135**(1046), 048003 (2023) <https://doi.org/10.1088/1538-3873/acbe66>
- [125] Pontoppidan, K.M., Pickering, T.E., Laidler, V.G., Gilbert, K., Sontag, C.D., Slocum, C., Sienkiewicz, M.J., Hanley, C., Earl, N.M., Pueyo, L., Ravindranath, S., Karakla, D.M., Roberto, M., Noriega-Crespo, A., Barker, E.A.: Pandeia: A multi-mission exposure time calculator for JWST and WFIRST. In: *Observatory Operations: Strategies, Processes, And Systems VI*, vol. 9910. eprint: arXiv:1707.02202, p. 991016 (2016). <https://doi.org/10.1117/12.2231768> . <https://ui.adsabs.harvard.edu/abs/2016SPIE.9910E..16P>
- [126] JWST Calibration Pipeline. <https://zenodo.org/records/17101851>
- [127] Greenfield, P., Miller, T.: The Calibration Reference Data System. *Astron. Comput.* **16**, 41–53 (2016) <https://doi.org/10.1016/j.ascom.2016.04.001>
- [128] Willott, C.J., Doyon, R., Albert, L., Brammer, G.B., Dixon, W.V., Muzic, K., Ravindranath, S., Scholz, A., Abraham, R., Artigau, É., Bradač, M., Goudfrooij, P., Hutchings, J.B., Iyer, K.G., Jayawardhana, R., LaMassa, S., Martis, N., Meyer, M.R., Morishita, T., Mowla, L., Muzzin, A., Noirot, G., Pacifici, C., Rowlands, N., Sarrouh, G., Sawicki, M., Taylor, J.M., Volk, K., Zabl, J.: The Near-infrared Imager and Slitless Spectrograph for the James Webb Space Telescope. II. Wide Field Slitless Spectroscopy. *Publ. Astron. Soc. Pac.* **134**(1032), 025002 (2022) <https://doi.org/10.1088/1538-3873/ac5158>
- [129] Rigby, J.R., Lightsey, P.A., García Marín, M., Bowers, C.W., Smith, E.C., Glasse, A., McElwain, M.W., Rieke, G.H., Chary, R.-R., Liu, X.C., Clampin, M., Kimble, R.A., Kinzel, W., Laidler, V., Mehalick, K.I., Noriega-Crespo, A., Shivaie, I., Skelton, D., Stark, C., Temim, T., Wei, Z., Willott, C.J.: How Dark the Sky: The JWST Backgrounds. *PASP* **135**(1046), 048002 (2023) <https://doi.org/10.1088/1538-3873/acbcf4>
- [130] Aniano, G., Draine, B.T., Gordon, K.D., Sandstrom, K.: Common-Resolution Convolution Kernels for Space- and Ground-Based Telescopes. *Publ. Astron. Soc. Pac.* **123**(908), 1218 (2011) <https://doi.org/10.1086/662219>
- [131] Perrin, M.D., Sivaramakrishnan, A., Lajoie, C.-P., Elliott, E., Pueyo, L., Ravindranath, S., Albert, Loïc.: Updated point spread function simulations for JWST with WebbPSF. In: Oschmann, Jr. Jacobus M., Clampin, M., Fazio, G.G., MacEwen, H.A. (eds.) *Space Telesc. Instrum. 2014 Opt. Infrared Millim. Wave. Society of Photo-Optical Instrumentation Engineers (SPIE) Conference Series*, vol. 9143, p. 91433 (2014). <https://doi.org/10.1117/12.2056689>
- [132] Libralato, M., Argyriou, I., Dicken, D., García Marín, M., Guillard, P., Hines, D.C., Kavanagh, P.J., Kendrew, S., Law, D.R., Noriega-Crespo, A., Álvarez-Márquez, J.: High-precision Astrometry and Photometry with the JWST/MIRI Imager. *Publ. Astron. Soc. Pac.* **136**, 034502 (2024) <https://doi.org/10.1088/1538-3873/ad2551>
- [133] Bolatto, A.D., Levy, R.C., Tarantino, E., Boyer, M.L., Fisher, D.B., Cronin, S.A., Leroy, A.K., Klessen, R.S., Smith, J.D., Berg, D.A., Böker, T., Boogaard, L.A., Ostriker, E.C., Thompson, T.A., Ott, J., Lenkić, L., Lopez, L.A., Dale, D.A., Veilleux, S., van der Werf, P.P., Glover, S.C.O., Sandstrom, K.M., Skillman, E.D., Chisholm, J., Villanueva, V., Lai, T.S.-Y., Lopez, S., Mills, E.A.C., Emig, K.L., Armus, L., Mayya, D., Meier, D.S., De Looze, I., Herrera-Camus, R., Walter, F., Relaño, M., Koziol, H.B., Marvil, J., Jiménez-Donaire, M.J., Martini, P.: JWST Observations of Starbursts: Polycyclic Aromatic Hydrocarbon Emission at the Base of the M82 Galactic Wind. *Astrophys. J.* **967**(1), 63 (2024) <https://doi.org/10.3847/1538-4357/ad33c8>
- [134] Chown, R., Okada, Y., Peeters, E., Sidhu, A., Khan, B., Schefter, B., Trahin, B., Canin, A., Van De Putte, D., Alarcón, F., Schroetter, I., Kannavou, O., Habart, E., Berné, O., Boersma, C., Cami, J., Dartois, E., Goicoechea, J., Gordon, K., Onaka, T.: PDRs4All: XIII. Empirical prescriptions

- for the interpretation of JWST imaging observations of star-forming regions. *Astron. Astrophys.* **698**, 86 (2025) <https://doi.org/10.1051/0004-6361/202452940>
- [135] Donnelly, G.P., Lai, T.S.-Y., Armus, L., Díaz-Santos, T., Larson, K.L., Barcos-Muñoz, L., Bianchin, M., Bohn, T., Böker, T., Buiten, V.A., Charmandaris, V., Evans, A.S., Howell, J., Inami, H., Kakkad, D., Lenkić, L., Linden, S.T., Lofaro, C.M., Malkan, M.A., Medling, A.M., Privon, G.C., Ricci, C., Smith, J.D.T., Song, Y., Stierwalt, S., van der Werf, P.P., U, V.: A Spectroscopically Calibrated Prescription for Extracting Polycyclic Aromatic Hydrocarbon Flux from JWST MIRI Imaging. *Astrophys. J.* **983**, 79 (2025) <https://doi.org/10.3847/1538-4357/adb97f>
 - [136] Joblin, C., Tielens, A.G.G.M., Allamandola, L.J., Geballe, T.R.: Spatial Variation of the 3.29 and 3.40 Micron Emission Bands within Reflection Nebulae and the Photochemical Evolution of Methylated Polycyclic Aromatic Hydrocarbons. *Astrophys. J.* **458**, 610 (1996) <https://doi.org/10.1086/176843>
 - [137] Hammonds, M., Mori, T., Usui, F., Onaka, T.: Variations in the 3.3 μm feature and carbonaceous dust in AKARI data. *Planet. Space Sci.* **116**, 73–83 (2015) <https://doi.org/10.1016/j.pss.2015.05.010>
 - [138] Boersma, C., Allamandola, L.J., Esposito, V.J., Maragkoudakis, A., Bregman, J.D., Temi, P., Lee, T.J., Fortenberry, R.C., Peeters, E.: JWST: Deuterated PAHs, PAH Nitriles, and PAH Overtone and Combination Bands. I. Program Description and First Look. *Astrophys. J.* **959**, 74 (2023) <https://doi.org/10.3847/1538-4357/ad022b>
 - [139] Allamandola, L.J., Boersma, C., Lee, T.J., Bregman, J.D., Temi, P.: PAH Spectroscopy from 1 to 5 M_{\odot} . *Astrophys. J.* **917**, 35 (2021) <https://doi.org/10.3847/2041-8213/ac17f0>
 - [140] Esposito, V.J., Allamandola, L.J., Boersma, C., Bregman, J.D., Fortenberry, R.C., Maragkoudakis, A., Temi, P.: Anharmonic IR absorption spectra of the prototypical interstellar PAHs phenanthrene, pyrene, and pentacene in their neutral and cation states. *Mol. Phys.* **122**(7-8), 2252936 (2024) <https://doi.org/10.1080/00268976.2023.2252936>
 - [141] Whitcomb, C.M., Sandstrom, K., Smith, J.-D.T.: JWST-MIRI Synthetic Photometry Composition using 460 Spitzer-IRS Spectra of Nearby Galaxies. *Res. Notes AAS* **7**(3), 38 (2023) <https://doi.org/10.3847/2515-5172/acc073>
 - [142] Misselt, K., Witt, A.N., Gordon, K.D., Van De Putte, D., Trahin, B., Abergel, A., Noriega-Crespo, A., Guillard, P., Zannese, M., Dell’ova, P., Baes, M., Klaassen, P., Ysard, N.: JWST observations of photodissociation regions: I. Aliphatic and aromatic carbonaceous dust, ices, and gas-phase spectral line inventory. *Astron. Astrophys.* **700**, 158 (2025) <https://doi.org/10.1051/0004-6361/202554851>
 - [143] Williams, T.G., Lee, J.C., Larson, K.L., Leroy, A.K., Sandstrom, K., Schinnerer, E., Thilker, D.A., Belfiore, F., Egorov, O.V., Rosolowsky, E., Sutter, J., DePasquale, J., Pagan, A., Berger, T.A., Anand, G.S., Barnes, A.T., Bigiel, F., Boquien, M., Cao, Y., Chastenot, J., Chevance, M., Chown, R., Dale, D.A., Deger, S., Eibensteiner, C., Emsellem, E., Faesi, C.M., Glover, S.C.O., Grasha, K., Hannon, S., Hassani, H., Henshaw, J.D., Jiménez-Donaire, M.J., Kim, J., Klessen, R.S., Koch, E.W., Li, J., Liu, D., Meidt, S.E., Méndez-Delgado, J.E., Murphy, E.J., Neumann, J., Neumann, L., Neumayer, N., Oakes, E.K., Pathak, D., Pety, J., Pinna, F., Querejeta, M., Ramambason, L., Romanelli, A., Sormani, M.C., Stuber, S.K., Sun, J., Teng, Y.-H., Usero, A., Watkins, E.J., Weinbeck, T.D.: PHANGS-JWST: Data-processing Pipeline and First Full Public Data Release. *Astrophys. J. Suppl. Ser.* **273**, 13 (2024) <https://doi.org/10.3847/1538-4365/ad4be5>
 - [144] Hagen, L.M.Z., Siegel, M.H., Hoversten, E.A., Gronwall, C., Immler, S., Hagen, A.: Swift Ultraviolet Survey of the Magellanic Clouds (SUMaC) - I. Shape of the ultraviolet dust extinction law and recent star formation history of the Small Magellanic Cloud. *Mon. Not. R. Astron. Soc.* **466**, 4540–4557 (2017) <https://doi.org/10.1093/mnras/stw2954>

- [145] Rosolowsky, E.W., Pineda, J.E., Kauffmann, J., Goodman, A.A.: Structural Analysis of Molecular Clouds: Dendrograms. *Astrophys. J.* **679**, 1338–1351 (2008) <https://doi.org/10.1086/587685>
- [146] Goodman, A.A., Rosolowsky, E.W., Borkin, M.A., Foster, J.B., Halle, M., Kauffmann, J., Pineda, J.E.: A role for self-gravity at multiple length scales in the process of star formation. *Nature* **457**, 63–66 (2009) <https://doi.org/10.1038/nature07609>
- [147] Kirk, J.M., Ward-Thompson, D., Palmeirim, P., André, Ph., Griffin, M.J., Hargrave, P.J., Könyves, V., Bernard, J.-P., Nutter, D.J., Sibthorpe, B., Di Francesco, J., Abergel, A., Arzoumanian, D., Benedettini, M., Bontemps, S., Elia, D., Hennemann, M., Hill, T., Men'shchikov, A., Motte, F., Nguyen-Luong, Q., Peretto, N., Pezzuto, S., Rygl, K.L.J., Sadavoy, S.I., Schisano, E., Schneider, N., Testi, L., White, G.: First results from the Herschel Gould Belt Survey in Taurus. *Mon. Not. R. Astron. Soc.* **432**, 1424–1433 (2013) <https://doi.org/10.1093/mnras/stt561>
- [148] Lind-Thomsen, C., Sneppen, A., Steinhardt, C.L.: A Power Spectral Study of PHANGS Galaxies with JWST MIRI: On the Spatial Scales of Dust and Polycyclic Aromatic Hydrocarbons. *Astrophys. J.* **985**, 144 (2025) <https://doi.org/10.3847/1538-4357/adc808>
- [149] Gordon, K.D., Bohlin, R., Sloan, G.C., Rieke, G., Volk, K., Boyer, M., Muzerolle, J., Schlawin, E., Deustua, S.E., Hines, D.C., Kraemer, K.E., Mullally, S.E., Su, K.Y.L.: The James Webb Space Telescope Absolute Flux Calibration. I. Program Design and Calibrator Stars. *Astron. J.* **163**, 267 (2022) <https://doi.org/10.3847/1538-3881/ac66dc>
- [150] Hensley, B.S., Draine, B.T.: The AstroDust+PAH Model: A Unified Description of the Extinction, Emission, and Polarization from Dust in the Diffuse Interstellar Medium. *Astrophys. J.* **948**(1), 55 (2023) <https://doi.org/10.3847/1538-4357/acc4c2>
- [151] Dalcanton, J.J., Fouesneau, M., Hogg, D.W., Lang, D., Leroy, A.K., Gordon, K.D., Sandstrom, K., Weisz, D.R., Williams, B.F., Bell, E.F., Dong, H., Gilbert, K.M., Gouliermis, D.A., Guhathakurta, P., Lauer, T.R., Schrubba, A., Seth, A.C., Skillman, E.D.: The Panchromatic Hubble Andromeda Treasury. VIII. A Wide-area, High-resolution Map of Dust Extinction in M31. *Astrophys. J.* **814**, 3 (2015) <https://doi.org/10.1088/0004-637X/814/1/3>
- [152] Gordon, K.D., Fouesneau, M., Arab, H., Tchernyshyov, K., Weisz, D.R., Dalcanton, J.J., Williams, B.F., Bell, E.F., Bianchi, L., Boyer, M., Choi, Y., Dolphin, A., Girardi, L., Hogg, D.W., Kalirai, J.S., Kapala, M., Lewis, A.R., Rix, H.-W., Sandstrom, K., Skillman, E.D.: The Panchromatic Hubble Andromeda Treasury. XV. The BEAST: Bayesian Extinction and Stellar Tool. *Astrophys. J.* **826**, 104 (2016) <https://doi.org/10.3847/0004-637X/826/2/104>
- [153] Lindberg, C.W., Murray, C.E., Yanchulova Merica-Jones, P., Bot, C., Burhenne, C., Choi, Y., Clark, C.J.R., Cohen, R.E., Gilbert, K.M., Goldman, S.R., Gordon, K.D., Hirschauer, A.S., McQuinn, K.B.W., Roman-Duval, J.C., Sandstrom, K.M., Tarantino, E., Williams, B.F.: Scylla. IV. Intrinsic Stellar Properties and Line-of-sight Dust Extinction Measurements toward 1.5 Million Stars in the SMC and LMC. *Astrophys. J.* **982**, 33 (2025) <https://doi.org/10.3847/1538-4357/adb4e8>